DESY–98–107

hep–ex/9808020

Exclusive Electroproduction of ρ^0 and J/ψ Mesons at HERA

ZEUS Collaboration

Abstract

Exclusive production of ρ^0 and J/ψ mesons in e^+p collisions has been studied with the ZEUS detector in the kinematic range $0.25 < Q^2 < 50\,\mathrm{GeV}^2$, $20 < W < 167\,\mathrm{GeV}$ for the ρ^0 data and $2 < Q^2 < 40\,\mathrm{GeV}^2$, $50 < W < 150\,\mathrm{GeV}$ for the J/ψ data. Cross sections for exclusive ρ^0 and J/ψ production have been measured as a function of Q^2, W and t. The spin-density matrix elements r^{04}_{00}, r^{1}_{1-1} and $\mathrm{Re}\, r^{5}_{10}$ have been determined for exclusive ρ^0 production as well as r^{04}_{00} and r^{04}_{1-1} for exclusive J/ψ production. The results are discussed in the context of theoretical models invoking soft and hard phenomena.

The ZEUS Collaboration

J. Breitweg, S. Chekanov, M. Derrick, D. Krakauer, S. Magill, D. Mikunas, B. Musgrave, J. Repond, R. Stanek, R.L. Talaga, R. Yoshida, H. Zhang
Argonne National Laboratory, Argonne, IL, USA [p]

M.C.K. Mattingly
Andrews University, Berrien Springs, MI, USA

F. Anselmo, P. Antonioli, G. Bari, M. Basile, L. Bellagamba, D. Boscherini, A. Bruni, G. Bruni, G. Cara Romeo, G. Castellini[1], L. Cifarelli[2], F. Cindolo, A. Contin, N. Coppola, M. Corradi, S. De Pasquale, P. Giusti, G. Iacobucci, G. Laurenti, G. Levi, A. Margotti, T. Massam, R. Nania, F. Palmonari, A. Pesci, A. Polini, G. Sartorelli, Y. Zamora Garcia[3], A. Zichichi
University and INFN Bologna, Bologna, Italy [f]

C. Amelung, A. Bornheim, I. Brock, K. Coböken, J. Crittenden, R. Deffner, M. Eckert, M. Grothe[4], H. Hartmann, K. Heinloth, L. Heinz, E. Hilger, H.-P. Jakob, A. Kappes, U.F. Katz, R. Kerger, E. Paul, M. Pfeiffer, H. Schnurbusch, A. Weber, H. Wieber
Physikalisches Institut der Universität Bonn, Bonn, Germany [c]

D.S. Bailey, W.N. Cottingham, B. Foster, R. Hall-Wilton, G.P. Heath, H.F. Heath, J.D. McFall,
D. Piccioni, D.G. Roff, J. Scott, R.J. Tapper
H.H. Wills Physics Laboratory, University of Bristol, Bristol, U.K. [o]

M. Capua, L. Iannotti, A. Mastroberardino, M. Schioppa, G. Susinno
Calabria University, Physics Dept.and INFN, Cosenza, Italy [f]

J.Y. Kim, J.H. Lee, I.T. Lim, M.Y. Pac[5]
Chonnam National University, Kwangju, Korea [h]

A. Caldwell[6], N. Cartiglia, Z. Jing, W. Liu, B. Mellado, J.A. Parsons, S. Ritz[7], S. Sampson, F. Sciulli, P.B. Straub, Q. Zhu
Columbia University, Nevis Labs., Irvington on Hudson, N.Y., USA [q]

P. Borzemski, J. Chwastowski, A. Eskreys, J. Figiel, K. Klimek, M.B. Przybycień, L. Zawiejski
Inst. of Nuclear Physics, Cracow, Poland [j]

L. Adamczyk[8], B. Bednarek, M. Bukowy, A.M. Czermak, K. Jeleń, D. Kisielewska, T. Kowalski,
M. Przybycień, E. Rulikowska-Zarębska, L. Suszycki, J. Zając
Faculty of Physics and Nuclear Techniques, Academy of Mining and Metallurgy, Cracow, Poland [j]

Z. Duliński, A. Kotański
Jagellonian Univ., Dept. of Physics, Cracow, Poland [k]

G. Abbiendi[9], L.A.T. Bauerdick, U. Behrens, H. Beier[10], J.K. Bienlein, K. Desler, G. Drews, U. Fricke, F. Goebel, P. Göttlicher, R. Graciani, T. Haas, W. Hain, G.F. Hartner, D. Hasell[11], K. Hebbel, K.F. Johnson[12], M. Kasemann, W. Koch, U. Kötz, H. Kowalski, L. Lindemann, B. Löhr, M. Martínez, J. Milewski[13], M. Milite, T. Monteiro[14], D. Notz, A. Pellegrino, F. Pelucchi, K. Piotrzkowski, M. Rohde, J. Roldán[15], J.J. Ryan[16], P.R.B. Saull, A.A. Savin, U. Schneekloth, O. Schwarzer, F. Selonke, M. Sievers, S. Stonjek, B. Surrow[14], E. Tassi, D. Westphal[17], G. Wolf, U. Wollmer, C. Youngman, W. Zeuner
Deutsches Elektronen-Synchrotron DESY, Hamburg, Germany

B.D. Burow, C. Coldewey, H.J. Grabosch, A. Meyer, S. Schlenstedt
DESY-IfH Zeuthen, Zeuthen, Germany

G. Barbagli, E. Gallo, P. Pelfer
University and INFN, Florence, Italy [f]

G. Maccarrone, L. Votano
INFN, Laboratori Nazionali di Frascati, Frascati, Italy [f]

A. Bamberger, S. Eisenhardt, P. Markun, H. Raach, T. Trefzger[18], S. Wölfle
Fakultät für Physik der Universität Freiburg i.Br., Freiburg i.Br., Germany [c]

J.T. Bromley, N.H. Brook, P.J. Bussey, A.T. Doyle[19], S.W. Lee, N. Macdonald, G.J. McCance, D.H. Saxon,
L.E. Sinclair, I.O. Skillicorn, E. Strickland, R. Waugh
Dept. of Physics and Astronomy, University of Glasgow, Glasgow, U.K. [o]

I. Bohnet, N. Gendner, U. Holm, A. Meyer-Larsen, H. Salehi, K. Wick
Hamburg University, I. Institute of Exp. Physics, Hamburg, Germany [c]

A. Garfagnini, I. Gialas[20], L.K. Gladilin[21], D. Kçira[22], R. Klanner, E. Lohrmann, G. Poelz, F. Zetsche
Hamburg University, II. Institute of Exp. Physics, Hamburg, Germany [c]

T.C. Bacon, I. Butterworth, J.E. Cole, G. Howell, L. Lamberti[23], K.R. Long, D.B. Miller, N. Pavel, A. Prinias[24], J.K. Sedgbeer, D. Sideris, R. Walker
Imperial College London, High Energy Nuclear Physics Group, London, U.K. [o]

U. Mallik, S.M. Wang, J.T. Wu[25]
University of Iowa, Physics and Astronomy Dept., Iowa City, USA [p]

P. Cloth, D. Filges
Forschungszentrum Jülich, Institut für Kernphysik, Jülich, Germany

J.I. Fleck[14], T. Ishii, M. Kuze, I. Suzuki[26], K. Tokushuku, S. Yamada, K. Yamauchi, Y. Yamazaki[27]
Institute of Particle and Nuclear Studies, KEK, Tsukuba, Japan [g]

S.J. Hong, S.B. Lee, S.W. Nam[28], S.K. Park
Korea University, Seoul, Korea [h]

H. Lim, I.H. Park, D. Son
Kyungpook National University, Taegu, Korea [h]

F. Barreiro, J.P. Fernández, G. García, C. Glasman[29], J.M. Hernández[30], L. Hervás[14], L. Labarga, J. del Peso, J. Puga, I. Redondo, J. Terrón, J.F. de Trocóniz
Univer. Autónoma Madrid, Depto de Física Teórica, Madrid, Spain [n]

F. Corriveau, D.S. Hanna, J. Hartmann, W.N. Murray, A. Ochs, M. Riveline, D.G. Stairs, M. St-Laurent
McGill University, Dept. of Physics, Montréal, Québec, Canada [a], [b]

T. Tsurugai
Meiji Gakuin University, Faculty of General Education, Yokohama, Japan

V. Bashkirov, B.A. Dolgoshein, A. Stifutkin
Moscow Engineering Physics Institute, Moscow, Russia [l]

G.L. Bashindzhagyan, P.F. Ermolov, Yu.A. Golubkov, L.A. Khein, N.A. Korotkova, I.A. Korzhavina, V.A. Kuzmin, O.Yu. Lukina, A.S. Proskuryakov, L.M. Shcheglova[31], A.N. Solomin[31], S.A. Zotkin
Moscow State University, Institute of Nuclear Physics, Moscow, Russia [m]

C. Bokel, M. Botje, N. Brümmer, J. Engelen, E. Koffeman, P. Kooijman, A. van Sighem, H. Tiecke, N. Tuning, W. Verkerke, J. Vossebeld, L. Wiggers, E. de Wolf
NIKHEF and University of Amsterdam, Amsterdam, Netherlands [i]

D. Acosta[32], B. Bylsma, L.S. Durkin, J. Gilmore, C.M. Ginsburg, C.L. Kim, T.Y. Ling, P. Nylander, T.A. Romanowski[33]
Ohio State University, Physics Department, Columbus, Ohio, USA [p]

H.E. Blaikley, R.J. Cashmore, A.M. Cooper-Sarkar, R.C.E. Devenish, J.K. Edmonds, J. Große-Knetter[34], N. Harnew, C. Nath, V.A. Noyes[35], A. Quadt, O. Ruske, J.R. Tickner[36], R. Walczak, D.S. Waters
Department of Physics, University of Oxford, Oxford, U.K. [o]

A. Bertolin, R. Brugnera, R. Carlin, F. Dal Corso, U. Dosselli, S. Limentani, M. Morandin, M. Posocco, L. Stanco, R. Stroili, C. Voci
Dipartimento di Fisica dell' Università and INFN, Padova, Italy [f]

B.Y. Oh, J.R. Okrasiński, W.S. Toothacker, J.J. Whitmore
Pennsylvania State University, Dept. of Physics, University Park, PA, USA [q]

Y. Iga
Polytechnic University, Sagamihara, Japan [g]

G. D'Agostini, G. Marini, A. Nigro, M. Raso
Dipartimento di Fisica, Univ. 'La Sapienza' and INFN, Rome, Italy [f]

J.C. Hart, N.A. McCubbin, T.P. Shah
Rutherford Appleton Laboratory, Chilton, Didcot, Oxon, U.K. [o]

D. Epperson, C. Heusch, J.T. Rahn, H.F.-W. Sadrozinski, A. Seiden, R. Wichmann, D.C. Williams
University of California, Santa Cruz, CA, USA [p]

H. Abramowicz[37], G. Briskin[38], S. Dagan[39], S. Kananov[39], A. Levy[39]
Raymond and Beverly Sackler Faculty of Exact Sciences, School of Physics, Tel-Aviv University,
Tel-Aviv, Israel [e]

T. Abe, T. Fusayasu, M. Inuzuka, K. Nagano, K. Umemori, T. Yamashita
Department of Physics, University of Tokyo, Tokyo, Japan [g]

R. Hamatsu, T. Hirose, K. Homma[40], S. Kitamura[41], T. Matsushita, T. Nishimura
Tokyo Metropolitan University, Dept. of Physics, Tokyo, Japan [g]

M. Arneodo[19], R. Cirio, M. Costa, M.I. Ferrero, S. Maselli, V. Monaco, C. Peroni, M.C. Petrucci, M. Ruspa, R. Sacchi, A. Solano, A. Staiano
Università di Torino, Dipartimento di Fisica Sperimentale and INFN, Torino, Italy [f]

M. Dardo
II Faculty of Sciences, Torino University and INFN - Alessandria, Italy [f]

D.C. Bailey, C.-P. Fagerstroem, R. Galea, K.K. Joo, G.M. Levman, J.F. Martin, R.S. Orr, S. Polenz, A. Sabetfakhri, D. Simmons
University of Toronto, Dept. of Physics, Toronto, Ont., Canada [a]

J.M. Butterworth, C.D. Catterall, M.E. Hayes, E.A. Heaphy, T.W. Jones, J.B. Lane, R.L. Saunders, M.R. Sutton, M. Wing
University College London, Physics and Astronomy Dept., London, U.K. [o]

J. Ciborowski, G. Grzelak[42], R.J. Nowak, J.M. Pawlak, R. Pawlak, B. Smalska, T. Tymieniecka,
A.K. Wróblewski, J.A. Zakrzewski, A.F. Żarnecki
Warsaw University, Institute of Experimental Physics, Warsaw, Poland [j]

M. Adamus
Institute for Nuclear Studies, Warsaw, Poland [j]

O. Deppe, Y. Eisenberg[39], D. Hochman, U. Karshon[39]
Weizmann Institute, Department of Particle Physics, Rehovot, Israel [d]

W.F. Badgett, D. Chapin, R. Cross, C. Foudas, S. Mattingly, D.D. Reeder, W.H. Smith, A. Vaiciulis, T. Wildschek, M. Wodarczyk
University of Wisconsin, Dept. of Physics, Madison, WI, USA [p]

A. Deshpande, S. Dhawan, V.W. Hughes
Yale University, Department of Physics, New Haven, CT, USA [p]

S. Bhadra, W.R. Frisken, M. Khakzad, W.B. Schmidke
York University, Dept. of Physics, North York, Ont., Canada [a]

[1] also at IROE Florence, Italy
[2] now at Univ. of Salerno and INFN Napoli, Italy
[3] supported by Worldlab, Lausanne, Switzerland
[4] now at University of California, Santa Cruz, USA
[5] now at Dongshin University, Naju, Korea
[6] also at DESY
[7] Alfred P. Sloan Foundation Fellow
[8] supported by the Polish State Committee for Scientific Research, grant No. 2P03B14912
[9] now at INFN Bologna
[10] now at Innosoft, Munich, Germany
[11] now at Massachusetts Institute of Technology, Cambridge, MA, USA
[12] visitor from Florida State University
[13] now at ATM, Warsaw, Poland
[14] now at CERN
[15] now at IFIC, Valencia, Spain
[16] now a self-employed consultant
[17] now at Bayer A.G., Leverkusen, Germany
[18] now at ATLAS Collaboration, Univ. of Munich
[19] also at DESY and Alexander von Humboldt Fellow at University of Hamburg
[20] visitor of Univ. of Crete, Greece, partially supported by DAAD, Bonn - Kz. A/98/16764
[21] on leave from MSU, supported by the GIF, contract I-0444-176.07/95
[22] supported by DAAD, Bonn - Kz. A/98/12712
[23] supported by an EC fellowship
[24] PPARC Post-doctoral fellow
[25] now at Applied Materials Inc., Santa Clara
[26] now at Osaka Univ., Osaka, Japan
[27] supported by JSPS Postdoctoral Fellowships for Research Abroad
[28] now at Wayne State University, Detroit
[29] supported by an EC fellowship number ERBFMBICT 972523
[30] now at HERA-B/DESY supported by an EC fellowship No.ERBFMBICT 982981
[31] partially supported by the Foundation for German-Russian Collaboration DFG-RFBR (grant no. 436 RUS 113/248/3 and no. 436 RUS 113/248/2)
[32] now at University of Florida, Gainesville, FL, USA
[33] now at Department of Energy, Washington
[34] supported by the Feodor Lynen Program of the Alexander von Humboldt foundation
[35] Glasstone Fellow
[36] now at CSIRO, Lucas Heights, Sydney, Australia
[37] an Alexander von Humboldt Fellow at University of Hamburg
[38] now at Brown University, Providence, RI, USA
[39] supported by a MINERVA Fellowship
[40] now at ICEPP, Univ. of Tokyo, Tokyo, Japan
[41] present address: Tokyo Metropolitan College of Allied Medical Sciences, Tokyo 116, Japan
[42] supported by the Polish State Committee for Scientific Research, grant No. 2P03B09308

[a] supported by the Natural Sciences and Engineering Research Council of Canada (NSERC)
[b] supported by the FCAR of Québec, Canada
[c] supported by the German Federal Ministry for Education and Science, Research and Technology (BMBF), under contract numbers 057BN19P, 057FR19P, 057HH19P, 057HH29P
[d] supported by the MINERVA Gesellschaft für Forschung GmbH, the German Israeli Foundation, the U.S.-Israel Binational Science Foundation, and by the Israel Ministry of Science
[e] supported by the German-Israeli Foundation, the Israel Science Foundation, the U.S.-Israel Binational Science Foundation, and by the Israel Ministry of Science
[f] supported by the Italian National Institute for Nuclear Physics (INFN)
[g] supported by the Japanese Ministry of Education, Science and Culture (the Monbusho) and its grants for Scientific Research
[h] supported by the Korean Ministry of Education and Korea Science and Engineering Foundation
[i] supported by the Netherlands Foundation for Research on Matter (FOM)
[j] supported by the Polish State Committee for Scientific Research, grant No. 115/E-343/SPUB/P03/002/97, 2P03B10512, 2P03B10612, 2P03B14212, 2P03B10412
[k] supported by the Polish State Committee for Scientific Research (grant No. 2P03B08614) and Foundation for Polish-German Collaboration
[l] partially supported by the German Federal Ministry for Education and Science, Research and Technology (BMBF)
[m] supported by the Fund for Fundamental Research of Russian Ministry for Science and Education and by the German Federal Ministry for Education and Science, Research and Technology (BMBF)
[n] supported by the Spanish Ministry of Education and Science through funds provided by CICYT
[o] supported by the Particle Physics and Astronomy Research Council
[p] supported by the US Department of Energy
[q] supported by the US National Science Foundation

1 Introduction

We report measurements of exclusive electroproduction of ρ^0 and J/ψ mesons at electron-proton centre-of-mass energy of $\sqrt{s} = 300$ GeV using the ZEUS detector at HERA. The reaction ep $\rightarrow$ eVp, where V stands for a vector meson (ρ^0, ϕ, J/ψ), is a rich source of information on soft and hard diffractive processes as well as on the hadronic properties of the virtual photon [1].

Exclusive photoproduction of light vector mesons (ρ^0, ω and ϕ) has been studied in a wide range of the photon-proton centre-of-mass energy W both in fixed target experiments [2] and at HERA [3, 4, 5]. For $W \gtrsim 10$ GeV these reactions display features characteristic of a soft diffractive process: s-channel helicity conservation, cross sections rising weakly with W and a steep exponential t dependence, where t is the squared four-momentum transfer at the proton vertex. Such processes are well described within the framework of Regge phenomenology [6] and the Vector-Meson Dominance model (VMD) [7], where exclusive vector-meson (VM) production at high energies is assumed to proceed via the exchange of a Pomeron trajectory as shown in Fig. 1a. In this approach, the W and t dependences are coupled:

$$\frac{\mathrm{d}\sigma^{\gamma \mathrm{p}}}{\mathrm{d}|t|} \propto e^{-b_0|t|} \left(\frac{W^2}{W_0^2}\right)^{2(\alpha(t)-1)}, \qquad (1)$$

where $\alpha(t) = \alpha(0)+\alpha' t$, while b_0 and W_0 are process-dependent constants. Fits to hadron-hadron scattering data and photoproduction data give $\alpha(0) = 1.08$ and $\alpha' = 0.25$ GeV^2 [8]. The slope of the t distribution depends on the energy as $b = b_0 + 2\alpha' \ln(W^2/W_0^2)$ (often referred to as "shrinkage"), while the effective power of a W^δ dependence of the cross section (after integrating over t) is $\delta \simeq 4(\alpha(0)-1-\alpha'/b)$. Typically, values of $b \simeq 10$ GeV^{-2} are found in the photoproduction of light VMs, leading to $\delta \simeq 0.22$, in agreement with measurements. This approach fails to describe the recently measured energy dependence of the cross section for elastic J/ψ photoproduction at HERA [9, 10]. The measured slope of the $|t|$ distribution, $b_{J/\psi} \simeq 5$ GeV^{-2}, leads to a prediction of $\delta \simeq 0.14$, in contrast to the measured value of $\delta \simeq 0.9$.

Exclusive VM electroproduction at high values of Q^2 has been studied in fixed target experiments [11, 12, 13] and at HERA [14, 15]. The measurements indicate that the rise of the cross section with W is stronger than that expected from Regge theory although there are large uncertainties in the experimental data[14]. The Q^2 dependence of the cross section can be described by Q^{-2n} with $2 \lesssim n \lesssim 2.5$ and the $|t|$ dependence has a slope b between 4 and 8 GeV^{-2}. The vector mesons are found to be produced predominantly in the helicity 0 state, whereas in photoproduction the production is mainly in the helicity ± 1 states.

In models based on perturbative QCD (pQCD), $\gamma^\star \mathrm{p} \rightarrow \mathrm{Vp}$ scattering is viewed as a sequence of events separated in time in the proton rest frame [16], as depicted in Fig. 1b. The steps are: the photon fluctuates into a $\mathrm{q\bar{q}}$ state; the $\mathrm{q\bar{q}}$ pair scatters on the proton target; and, the scattered $\mathrm{q\bar{q}}$ pair turns into a vector meson. The interaction of the $\mathrm{q\bar{q}}$

pair with the proton is mediated in leading order by the exchange of two gluons in a colour singlet state. In this framework, the cross section is proportional to the square of the gluon density in the proton. The scale μ^2, at which α_s and the gluon density are evaluated, can depend on the mass of the vector meson M_V, on Q^2 and on t. For J/ψ production the scale $\mu^2 = [Q^2 + M^2_{J/\psi} + |t|]/4$ [17] has been proposed. In photoproduction at small $|t|$, the scale would therefore have the value $\mu^2 = 2.4$ GeV^2. At this scale, the gluon density at small x rises as $xg(x) \propto x^{-0.2}$ [18], yielding a W dependence of the cross section $\sigma^{\gamma p} \propto W^{0.8}$, significantly steeper than expected from VMD and Regge phenomenology. The calculation has been extended [19] and compared to HERA data. It was found that this process is indeed sensitive to the form of the gluon density in the proton. Other pQCD calculations have been performed within the framework of the Colour Dipole Model (CDM) [20] where diffraction is viewed as the elastic scattering of a colour dipole of definite size off the target proton.

At large Q^2, the cross section is predicted to be dominated by longitudinally polarised virtual photons scattering into vector mesons of helicity state 0 [16, 21, 22, 23]. The cross section, calculated in leading $\alpha_s \ln \frac{Q^2}{\Lambda^2} \ln \frac{1}{x}$ approximation [16] for vector mesons composed of light flavours, is

$$\left.\frac{\mathrm{d}\sigma_L^{\gamma^* p}}{\mathrm{d}|t|}\right|_{t=0} = \frac{A}{Q^6}\alpha_s^2(Q^2)\left|\left(1 + \frac{\mathrm{i}\pi}{2}\frac{\mathrm{d}}{\mathrm{d}\ln x}\right) xg(x,Q^2)\right|^2, \qquad (2)$$

where A is a constant which depends on the VM wavefunction. Here we discuss some of the expectations for the cross sections:

- The cross section contains a $1/Q^6$ factor. However, the Q^2 dependences of α_s and the gluon density also need to be taken into account. The effective Q^2 dependence using the CTEQ3L gluon density function [24] and the leading-order form for α_s is approximately $\mathrm{d}\sigma_L^{\gamma^* p}/\mathrm{d}|t| \propto 1/Q^5$, with a weak x dependence. The calculation presented in [16] has been redone in leading $\alpha_s \ln(Q^2/\Lambda^2)$ approximation [25]. In this work, among other improvements, the Fermi motion of the quarks in the vector meson has been considered. The net effect is to reduce the steepness of the Q^2 dependence. Precise measurements could therefore yield information on the wavefunctions of the vector mesons.

- In the pQCD calculations, the t and W dependences are not coupled, so that no shrinkage is expected. A lack of shrinkage, along with a steep W dependence, indicates that the reaction is predominantly driven by perturbative processes. In such processes, the transverse size of the $q\bar{q}$ pair is small, and the slope is determined by the proton size, resulting in a value for b near 5 GeV^{-2} [26].

- The cross section presented in Eq. 2 is for longitudinally polarised photons. The authors of ref. [16] expect that this is the dominant contribution to the cross section in DIS. It has been argued [22] that the region of validity of the pQCD calculations is signalled by the predominance of VM production in the helicity zero state. A recent pQCD calculation for ρ^0 electroproduction [27], based on the production of

light $q\bar{q}$ pairs and parton–hadron duality, gives an estimate of the transverse photon contribution to the $\gamma^* p \to \rho^0 p$ cross section.

- The interaction should be flavour-independent at sufficiently high scales. From the quark charges of the vector mesons and assuming a flavour-independent production mechanism, the exclusive production cross sections should be in the proportions $9:1:2:8$ for $\rho^0 : \omega : \phi : J/\psi$. This expectation is badly broken at low Q^2. The pQCD predictions change the ratio somewhat due to wavefunction effects, such that the relative contribution of heavier vector mesons is enhanced [25] at high Q^2.

In this paper, we investigate the dependence of ρ^0 and J/ψ production on the variables W, Q^2, and t. The ρ^0 and J/ψ mesons are identified via their decay to two oppositely charged particles. Invariant masses are reconstructed under the assumption of dipion final states for the ρ^0 and dimuon final states for the J/ψ. The decay angular distributions are also measured, and the helicity matrix elements extracted, yielding a measurement of $R = \sigma_L^{\gamma^* p}/\sigma_T^{\gamma^* p}$ as a function of Q^2 and W. The results are compared to expectations from Regge theory as well as from pQCD models. The data are presented for ρ^0 production in the ranges $0.25 < Q^2 < 0.85$ GeV^2 (BPC ρ^0) and $3 < Q^2 < 50$ GeV^2 (DIS ρ^0). The production of J/ψ mesons is investigated in the Q^2 range $2 < Q^2 < 40$ GeV^2 (DIS J/ψ). The data discussed in this paper correspond to integrated luminosities of 6.0 pb^{-1} (DIS ρ^0 and J/ψ) and 3.8 pb^{-1} (BPC ρ^0) collected in 1995.

2 Experiment

The measurements were performed at the DESY ep collider HERA using the ZEUS detector. In 1995 HERA operated at a proton energy of 820 GeV and a positron energy of 27.5 GeV. A detailed description of the ZEUS detector can be found elsewhere [28]. The main components used in this analysis are described below.

The high-resolution uranium-scintillator calorimeter CAL [29] consists of three parts: forward [1] (FCAL), barrel (BCAL) and rear (RCAL) calorimeters. Each part is subdivided transversely into towers which are segmented longitudinally into one electromagnetic section (EMC) and one (RCAL) or two (FCAL, BCAL) hadronic sections (HAC). The energy resolution of the calorimeter, determined in a test beam, is $\sigma_E/E = 0.18/\sqrt{E}$ for electrons and $\sigma_E/E = 0.35/\sqrt{E}$ for hadrons, where E is expressed in GeV.

Charged-particle tracks are reconstructed and their momenta determined using the central (CTD) [30] and rear tracking detectors (RTD) [28]. The CTD is a cylindrical drift chamber operated in a magnetic field of 1.43 T produced by a superconducting solenoid. It consists of 72 cylindrical layers, organised in 9 superlayers covering the polar angular region $15° <$

[1] Throughout this paper the standard ZEUS right-handed coordinate system is used: the Z-axis points in the direction of the proton beam momentum (referred to as the forward direction) and the horizontal X-axis points towards the centre of HERA. The nominal interaction point is at $X = Y = Z = 0$.

$\theta < 164°$. The RTD is a set of planar drift chambers located at the rear of the CTD, covering the polar angle region $162° < \theta < 170°$.

The positions of positrons scattered at small angles with respect to the beam direction are determined in the beam pipe calorimeter (BPC) and the small-angle rear tracking detector (SRTD).

The BPC is an electromagnetic sampling calorimeter consisting of 2 modules, placed one on each side of the beam pipe, 294 cm away from the nominal ep interaction point in the rear region. Each module is equipped with 26 tungsten plates (roughly 24 radiation lengths), separated by layers of scintillator fingers (strips) each 8 mm wide. The strips alternate in the horizontal and vertical orientation, providing two-dimensional position information. The energy and position resolutions for electrons in the BPC, measured in a test beam, were found to be $17\%/\sqrt{E}$ (E in GeV) and $\simeq 1$ mm, respectively.

The SRTD is attached to the front face of the RCAL. It consists of two planes of scintillator strips, 1 cm wide and 0.5 cm thick, arranged in orthogonal orientations and read out via optical fibres and photomultiplier tubes. It covers the region of 68×68 cm^2 in X and Y with the exclusion of a 10×20 cm^2 hole at the centre for the beam pipe. The SRTD has a position resolution of 0.3 cm.

The luminosity is determined from the rate of the Bethe-Heitler process $e^+p \to e^+\gamma p$, where the high-energy photon is measured with a lead-scintillator calorimeter (LUMI) located at $Z = -107$ m in the HERA tunnel downstream of the interaction point in the positron flight direction [31].

3 Kinematics and cross sections

We will use the following kinematic variables to describe exclusive VM production (see Fig. 1): k, k', P, P', q, the four-momenta of the incident positron, scattered positron, incident proton, scattered proton and virtual photon, respectively; $Q^2 = -q^2 = -(k-k')^2$, the negative four-momentum squared of the virtual photon; $W^2 = (q+P)^2$, the squared invariant mass of the photon-proton system; $y = (P\cdot q)/(P\cdot k)$, the fraction of the positron energy transferred to the photon in the proton rest frame; and, $t = (P-P')^2$, the squared four-momentum transfer at the proton vertex.

The kinematic variables were reconstructed with the so-called "constrained" method, which involves the momenta of the decay particles measured in the CTD and the polar and azimuthal angles of the scattered positron in the BPC (ρ^0 at low Q^2 only) or in the main ZEUS calorimeter and the SRTD (all high-Q^2 events). Neglecting the transverse momentum of the outgoing proton with respect to its incoming momentum, the energy of the scattered positron can be expressed as

$$E_{e'} \simeq [2E_e - (E_V - p_V^Z)]/(1 - \cos\theta_{e'}), \tag{3}$$

where $E_{\rm e}$ is the energy of the incident positron, $E_{\rm V}$ and $p_{\rm V}^Z$ are the energy and longitudinal momentum of the VM, and $\theta_{e'}$ is the polar angle of the scattered positron. The values of Q^2 and t were calculated according to

$$Q^2 = 2E_{e'}E_{\rm e}(1+\cos\theta_{e'}), \tag{4}$$

$$|t| = (p_{e'}^X + p_{\rm V}^X)^2 + (p_{e'}^Y + p_{\rm V}^Y)^2, \tag{5}$$

where $p_{e'}^X$, $p_{e'}^Y$ and $p_{\rm V}^X$, $p_{\rm V}^Y$ are the X and Y components of the momentum of the scattered positron and VM. The variable y was calculated according to the expression

$$y = (E_{\rm V} - p_{\rm V}^Z)/2E_{\rm e} \tag{6}$$

and Bjorken-x was evaluated using the relation $Q^2 = sxy$, where s is the squared ep centre of mass energy. The kinematic ranges covered by the data are shown in Fig. 2.

In the Born approximation, the positron-proton cross section can be expressed in terms of the transverse, $\sigma_{\rm T}^{\gamma^\star {\rm p}}$, and longitudinal, $\sigma_{\rm L}^{\gamma^\star {\rm p}}$, virtual photoproduction cross sections as

$$\frac{{\rm d}^2\sigma^{ep}}{{\rm d}y{\rm d}Q^2} = \Gamma_T(y,Q^2)(\sigma_{\rm T}^{\gamma^\star {\rm p}} + \epsilon\sigma_{\rm L}^{\gamma^\star {\rm p}}), \tag{7}$$

where Γ_T is the transverse photon flux and ϵ is the ratio of longitudinal and transverse photon fluxes, given by $\epsilon = 2(1-y)/(1+(1-y)^2)$. In the kinematic range of this analysis, the value of ϵ varies from 0.94 to 1.0. The transverse photon flux is [32]

$$\Gamma_T = \frac{\alpha}{2\pi}\frac{1+(1-y)^2}{yQ^2}, \tag{8}$$

where α is the fine-structure constant. The virtual photon-proton cross section $\sigma^{\gamma^\star {\rm p}} \equiv \sigma_{\rm T}^{\gamma^\star {\rm p}} + \epsilon\sigma_{\rm L}^{\gamma^\star {\rm p}}$ can be used to evaluate the total exclusive cross section, $\sigma_{\rm tot}^{\gamma^\star {\rm p}} \equiv \sigma_{\rm T}^{\gamma^\star {\rm p}} + \sigma_{\rm L}^{\gamma^\star {\rm p}}$, through the relation:

$$\sigma_{\rm tot}^{\gamma^\star {\rm p}} = \frac{1+R}{1+\epsilon R}\sigma^{\gamma^\star {\rm p}}, \tag{9}$$

where $R = \sigma_{\rm L}^{\gamma^\star {\rm p}}/\sigma_{\rm T}^{\gamma^\star {\rm p}}$ is the ratio of the cross sections for longitudinal and transverse photons.

At given values of W and Q^2, the exclusive production and decay of VMs is described by three angles: $\Phi_{\rm h}$ – the angle between the VM production plane and the positron scattering plane; $\theta_{\rm h}$ and $\phi_{\rm h}$ – the polar and azimuthal angles of the positively charged decay particle in the s-channel helicity frame, in which the spin quantisation axis is defined along the VM direction in the photon-proton centre-of-mass system. The angular distribution as a function of these three angles, $W(\cos\theta_{\rm h}, \phi_{\rm h}, \Phi_{\rm h})$, is described by the ρ^0 spin-density matrix elements, ρ_{ik}^α, where i,k=-1,0,1 and by convention α=0,1,2,4,5,6 for an unpolarised (or transversely polarised) electron beam [33]. The superscripts denote the decomposition of the spin-density matrix into contributions from the photon polarisation states: unpolarised transverse photons (0), linearly polarised transverse photons (1,2), longitudinally polarised photons (4), and from the interference of longitudinal and transverse amplitudes

(5,6). For given values of W and Q^2, the polarisation parameter ϵ is constant, so that the contributions from ρ^0_{ik} and ρ^4_{ik} cannot be distinguished. The decay angular distribution can therefore be expressed in terms of linear combinations of the density matrix elements, r^{04}_{ik} and r^{α}_{ik}, as

$$r^{04}_{ik} = \frac{\rho^0_{ik} + \epsilon R \rho^4_{ik}}{1 + \epsilon R}, \tag{10}$$

$$r^{\alpha}_{ik} = \begin{cases} \dfrac{\rho^{\alpha}_{ik}}{1 + \epsilon R}, & \alpha = 1, 2 \\ \dfrac{\sqrt{R}\,\rho^{\alpha}_{ik}}{1 + \epsilon R}, & \alpha = 5, 6. \end{cases} \tag{11}$$

Under the assumption of s-channel helicity conservation (SCHC), the angular distribution for the decay of the ρ^0 meson depends on only two angles, $\theta_{\rm h}$ and $\psi_{\rm h} = \phi_{\rm h} - \Phi_{\rm h}$, and is characterised by three independent parameters, r^{04}_{00}, r^1_{1-1} and Re r^5_{10}, as

$$\begin{aligned} W(\cos\theta_{\rm h}, \psi_{\rm h}) = \frac{3}{4\pi}[&\frac{1}{2}(1 - r^{04}_{00}) + \frac{1}{2}(3r^{04}_{00} - 1)\ \cos^2\theta_{\rm h} \\ &+ \epsilon r^1_{1-1} \sin^2\theta_{\rm h} \cos 2\psi_{\rm h}\ - 2\sqrt{\epsilon(1+\epsilon)}{\rm Re}(r^5_{10}) \sin 2\theta_{\rm h} \cos\psi_{\rm h}]. \end{aligned} \tag{12}$$

The ratio $R = \sigma^{\gamma^* {\rm p}}_{\rm L} / \sigma^{\gamma^* {\rm p}}_{\rm T}$ can be determined from the polar angle distribution via

$$R = \frac{1}{\epsilon} \frac{r^{04}_{00}}{1 - r^{04}_{00}}. \tag{13}$$

The additional assumption of natural-parity exchange in the t-channel reduces the number of independent parameters to two. The polar and azimuthal angle distributions are related via

$$r^1_{1-1} = \frac{1}{2}(1 - r^{04}_{00}), \tag{14}$$

independently of the value of R. These relations were found to hold for diffractive processes at low energy [34].

Statistical considerations limited our helicity analysis of the J/ψ sample to the one-dimensional distributions in $\theta_{\rm h}$ and $\phi_{\rm h}$, integrated over $\Phi_{\rm h}$. For the decay to spin-1/2 fermions, the above assumptions of SCHC and natural-parity exchange in the t-channel yield distributions sensitive to r^{04}_{00} and r^{04}_{1-1} according to

$$W(\cos\theta_{\rm h}) = \frac{3}{8}\left[1 + r^{04}_{00} + (1 - 3r^{04}_{00})\cos^2\theta_{\rm h}\right], \tag{15}$$

$$W(\cos\phi_{\rm h}) = \frac{1}{2\pi}\left[1 + r^{04}_{1-1}\cos 2\phi_{\rm h}\right]. \tag{16}$$

A value for R can be extracted from the polar angle distribution using Eq. 13.

4 Event selection

The online event selection is done with a three-level trigger system [35]. The exclusive reaction ep $\rightarrow$ eρ^0p at low Q^2 (BPC) was selected at the first trigger level by the requirement of an energy deposit in the BPC of more than 6 GeV and at least one track candidate in the CTD. The DIS ρ^0 and J/ψ trigger at the first level performed an initial identification of the scattered electron in the main calorimeter by looking for isolated energy deposits.

At the second trigger level general timing cuts were applied, along with a cut on the quantity $E - p_Z = \sum_i (E_i - p_{Z_i})$, where $E_i = \sqrt{p_{X,i}^2 + p_{Y,i}^2 + p_{Z,i}^2}$ denotes the energy in the i-th calorimeter cell. The latter cut rejected background from photoproduction events. The BPC trigger included a restriction on the number of tracks in the CTD.

At the third trigger level, requirements specific to the exclusive reaction were imposed. These requirements were similar to those applied offline and included a vertex cut, a limit on the maximum number of tracks reconstructed by the CTD and a restriction on the maximum energy in the inner rings of the FCAL (rejecting events with proton dissociation). In the case of the DIS ρ^0 and J/ψ events a positron candidate in the CAL was required and a fiducial cut on the positron position close to the rear beam pipe performed.

In the offline selection of the exclusive ρ^0 and J/ψ candidate events, the following further requirements were imposed:

- The energy of the scattered positron was required to be greater than 20 GeV if measured in the BPC and greater than 5 (DIS ρ^0) or 8 GeV (J/ψ) if measured in the uranium calorimeter. Positron identification in the latter two analyses used an algorithm based on a neural network [36]. The efficiency was greater than 96%. In the case of the BPC, cuts were imposed on the deposited energy, shower width, timing and the BPC fiducial region. With these cuts, the probability that a selected particle is a positron exceeds 99% [37].

- $E - p_Z > 40$ GeV. This cut, applied in both DIS analyses, excluded events requiring large radiative corrections.

- The Z coordinate of the interaction vertex was required to be within ± 50 cm of the nominal interaction point.

- In addition to the scattered positron the presence of two oppositely charged tracks was required, each associated with the reconstructed vertex, and each with pseudorapidity[2] $|\eta|$ less than 1.75 and transverse momentum greater than 150 MeV. These cuts excluded regions of low efficiency and poor momentum resolution in the tracking detectors.

[2] The pseudorapidity η is defined as $\eta = -\ln[\tan(\frac{\theta}{2})]$.

- A match between each of the aforementioned tracks and an energy deposit in the calorimeter was required. Energy deposits not associated with tracks or the positron were required to be less than than 300 MeV (elasticity cut), using a matching procedure developed for this analysis [38].

In addition, the following cuts were applied to select kinematic regions of high acceptance. The BPC ρ^0 analysis was limited to the region $0.25 < Q^2 < 0.85$ GeV^2 and $20 < W < 90$ GeV. The DIS ρ^0 analysis was restricted to the kinematic region $3 < Q^2 < 50$ GeV^2 and $32 < W < 167$ GeV. For the cross section calculation, only events in the $\pi^+\pi^-$ mass interval $0.6 < M_{\pi\pi} < 1.2$ GeV and with $|t| < 0.6$ GeV^2 were taken in both ρ^0 analyses. For the J/ψ analysis, cuts of $2 < Q^2 < 40$ GeV^2 and $50 < W < 150$ GeV were applied. Only events within the mass interval $2 < M_{l^+l^-} < 4$ GeV were accepted, where $M_{l^+l^-}$ was calculated using the muon mass for the J/ψ decay products.

The above selection procedure yielded 5462 events in the BPC ρ^0 sample, 3039 events in the DIS ρ^0 sample and 213 events in the J/ψ sample.

5 Acceptance corrections

In the BPC ρ^0 analysis, a dedicated Monte Carlo generator based on the JETSET [39] package was used to evaluate the acceptance and resolution of the ZEUS detector. The simulation of exclusive ρ^0 production was based on the VMD model and Regge phenomenology. Events were generated in the region $0.15 < Q^2 < 1.1$ GeV^2, and $15 < W < 110$ GeV. The effective Q^2, W and t dependences of the cross section were parameterised as $\sigma_{\rm tot}^{\gamma^\star {\rm p}} \propto 1/(1+Q^2/M_\rho^2)^{1.75}$, $\sigma_{\rm tot}^{\gamma^\star {\rm p}} \propto W^{0.12}$ and ${\rm d}\sigma^{\rm ep}/{\rm d}|t| = \exp(-b|t|+ct^2)$ ($b = 9$ GeV^{-2}, $c = 2$ GeV^{-4}), respectively. Decay angular distributions were generated assuming SCHC. A sample of events was generated using HERACLES [40] in order to evaluate the magnitude of radiative corrections in the BPC ρ^0 data. For the selected events they were found not to exceed 2% for any data point and to be consistent with zero within statistical errors. A 2% error was thus included in the normalisation uncertainty.

In the DIS ρ^0 analysis, a dedicated program [41] interfaced to HERACLES [40] was used to evaluate the acceptance and resolution associated with the "constrained" method of reconstruction. The cross section for exclusive ρ^0 production was parameterised in terms of $\sigma_{\rm L}^{\gamma^\star {\rm p}}$ and $\sigma_{\rm T}^{\gamma^\star {\rm p}}$ over the entire W and Q^2 range covered by the data. At high Q^2, initial-state radiation (ISR) introduces not only an overall correction to the cross section but also significantly distorts the distributions of certain kinematic variables. In the "constrained" method, ISR leads to migration of events along lines of constant W towards higher values of Q^2. Moreover, it leads to additional and biased smearing of the reconstructed value of t. (For a cut on $E - p_Z$ of 40 GeV, smearing due to ISR produces a decrease of the t slope by 5%). Final-state radiation does not introduce a significant error, as the radiated photon is usually well contained within the calorimeter cluster of the scattered positron.

In the DIS J/ψ analysis the Monte Carlo program DIPSI [42], based on the model of Ryskin [17], was used. In this model, the exchanged photon fluctuates into a $c\bar{c}$ pair

which subsequently interacts with a gluon ladder emitted by the incident proton, and SCHC is assumed. The longitudinal and transverse cross sections are related by $\sigma_{\rm L}^{\gamma^\star {\rm p}} = (Q^2/M_{J/\psi}^2)\,\sigma_{\rm T}^{\gamma^\star {\rm p}}$, where $M_{J/\psi}$ is the mass of vector meson J/ψ. For the gluon density in the proton the MRSA$'$ parameterisation was used [43]. Events were generated assuming an exponential t distribution $\exp(-b|t|)$ with $b = 5$ GeV^{-2}. The same method and tools as in the BPC ρ^0 analysis were used to calculate radiative corrections. Their magnitude was found not to exceed 4% for any data point and this value was included in the normalisation uncertainty.

Two other generators, PYTHIA and EPSOFT, were used for determination of the background from processes in which the proton dissociates. For the DIS ρ^0 and J/ψ analyses, the EPSOFT [44] Monte Carlo, developed in the framework of HERWIG [45], was used. It was assumed that the cross section for the reaction $\gamma^\star {\rm p} \to {\rm VN}$, where N denotes the hadronic final state originating from the dissociated proton, is of the form

$$\frac{{\rm d}^2\sigma^{\gamma^\star {\rm p}\to {\rm VN}}}{{\rm d}t\,{\rm d}M_{\rm N}^2} = \frac{1}{2}\frac{{\rm d}\sigma^{\gamma^\star {\rm p}\to {\rm Vp}}}{{\rm d}|t|}\left(\frac{{\rm d}\sigma^{\rm pp\to pN}}{{\rm d}t\,{\rm d}M_{\rm N}^2}\Big/\frac{{\rm d}\sigma^{\rm pp\to pp}}{{\rm d}t}\right), \qquad (17)$$

where the ratio $\frac{{\rm d}\sigma^{\rm pp\to pN}}{{\rm d}t{\rm d}M_{\rm N}^2}/\frac{{\rm d}\sigma^{\rm pp\to pp}}{{\rm d}t}$ is obtained from fits to pp data [44]. The PYTHIA generator [46] was used for the BPC analysis. A cross section of the form $\frac{{\rm d}^2\sigma^{\gamma^\star {\rm p}\to {\rm VN}}}{{\rm d}t{\rm d}M_{\rm N}^2} \propto e^{-b|t|}F_{\rm sd}(M_{\rm N})/M_{\rm N}^2$ is assumed in PYTHIA, with $b = b_0 + 2\alpha' \ln(W^2/M_{\rm N}^2)$, $b_0 = 2.8$ GeV^{-2} and $\alpha' = 0.25$ GeV^2, corresponding to an effective $b \simeq 5$ GeV^{-2} in the kinematic region of our results. The function $F_{\rm sd}(M_{\rm N})$ enhances the cross section in the low mass resonance region and suppresses the production of very large masses [46]. A fit to the generated $M_{\rm N}$ spectrum for $10 < M_{\rm N}^2 < 200$ GeV^2 with a function of the type $1/M_{\rm N}^n$ gives $n = 2.2$. The effect of the functions $F_{\rm sd}(M_{\rm N})$ and $b = b(M_{\rm N})$ on the spectrum is thus consistent with the result $n = 2.24 \pm 0.03$ measured for the diffractive dissociation of the proton in $\rm p\bar{p}$ collisions [47].

In all three analyses the generated events were processed through the same chain of selection and reconstruction procedures as the data, accounting for trigger as well as detector efficiencies and smearing effects in the ZEUS detector. The distributions of generated variables were reweighted so as to reproduce the measured distributions after reconstruction. Corrections for the data, evaluated on the basis of the Monte Carlo samples, were calculated independently in each bin of any given variable.

A comparison of data and MC simulation is presented in Fig. 3 (Q^2, W and $E_{e'}$), Fig. 4 (η and $p_{\rm T}$) and Fig. 5 ($\cos\theta_{\rm h}$ and $\psi_{\rm h}$). The J/ψ sample is restricted to the mass range $2.85 < M_{\rm l^+l^-} < 3.25$ GeV in order to reduce the contribution from hadron pairs. The dominant remaining background originates from the Bethe-Heitler process $\rm ep \to e\,l^+l^-\,p$, and this contribution is represented by the shaded areas in the respective figures. This process, where the lepton pairs are either electrons or a muons, proceeds via the fusion of a photon radiated by the incoming electron and one radiated by the proton. Single particle distributions are very sensitive to the correct simulation of the W, Q^2, t and decay angle variables. As an example, the transverse momentum distribution of the decay pion in the DIS ρ^0 sample (Fig. 4) displays a two-peak structure with maxima positioned around

~ 0.3 and ~ 1.8 GeV^2 (this shape is less distinct in the case of the BPC ρ^0s). Since at large values of Q^2 the ρ^0 mesons are predominantly produced in the helicity zero state, one of the decay pions is emitted along the direction of the ρ^0 while the other one is approximately at rest in the $\gamma^\star p$ centre-of-mass frame. This configuration results in the p_{T} spectrum, measured in the laboratory frame, shown in Fig. 4. The measured and simulated spectra of $\cos\theta_{\mathrm{h}}$ and ψ_{h} (for $|\cos\theta_{\mathrm{h}}| < 0.5$ and $|\cos\theta_{\mathrm{h}}| > 0.5$) are shown in Fig. 5. The polar and azimuthal angular distributions are strongly correlated and the observed agreement between the measured and the simulated distributions was obtained via careful tuning of the simulation.

6 Background

After applying the selection criteria described earlier, the data still contain contributions from various background processes:

- Proton-dissociative vector-meson production, ep $\rightarrow$ eVN, where N is a state of mass M_{N} into which the proton diffractively dissociates.
- Elastic production of ω and ϕ mesons (for the ρ^0 analyses) and of ψ' mesons (for the J/ψ analysis).
- Photon diffractive dissociation, ep $\rightarrow$ eXp and ep $\rightarrow$ eXN, in which the photon diffractively dissociates into a state X and the proton either remains intact or dissociates.
- Bethe-Heitler production of $\mathrm{e^+e^-}$ and $\mu^+\mu^-$ pairs.
- Beam-gas interactions.

The main source of background consists of events with the proton diffractively dissociating into hadrons. Some of the hadrons deposit energy around the beam pipe in the FCAL but a fraction escape detection. The contribution by this process to the observed yields was estimated by using exclusive VM events with an energy deposit of at least 0.4 GeV in the FCAL. (Contamination of this sample by DIS events is negligible.)

Fig. 6 shows the ratios of the Q^2, W, $\cos\theta_{\mathrm{h}}$ and t distributions for FCAL-tagged events to those for all events in the BPC ρ^0 sample. The fraction of FCAL-tagged events is approximately independent of Q^2, W and $\cos\theta_{\mathrm{h}}$. However, a significant dependence on t is observed. The latter is expected as a consequence of the different t dependences of the cross sections for elastic and proton-dissociative reactions. The same conclusions can be reached for the FCAL-tagged events from the DIS ρ^0 and J/ψ samples. Under the assumption that a tag in the FCAL does not affect the shape of the acceptance as a function of Q^2, W and $\cos\theta_{\mathrm{h}}$ (as indicated by PYTHIA and EPSOFT), this result suggests that proton-dissociative and elastic vector-meson production have the same Q^2,

W and $\cos\theta_{\rm h}$ distributions. This supports the hypothesis of factorisation of diffractive vertices [48]. Similar conclusions were reached earlier for ρ^0 production at $Q^2 \simeq 0$ [49] and in DIS [50].

In the BPC and DIS ρ^0 analyses the proton-dissociative background evaluation was performed by comparing the number of events with energy deposited in FCAL in the data and the proton dissociative EPSOFT or PYTHIA samples. Specifically, the number of residual proton-dissociative events in the data with FCAL energy smaller than the threshold E_0 (1 GeV for the BPC analysis and 0.4 GeV for the DIS ρ^0 analysis) was estimated as

$$N_{\rm pdiss}^{\rm DATA} = \left\{ \frac{N_{\rm pdiss}}{N(E_{\rm FCAL} > E_0)} \right\}^{\rm MC} \times \{N(E_{\rm FCAL} > E_0)\}^{\rm DATA} ,$$

where $N_{\rm pdiss}$ is the fraction of elastic events passing the final cuts. A total of 160 (64) FCAL-tagged events were used for the BPC ρ^0 (DIS ρ^0) analysis. In the BPC case, the additional requirement $W > 50$ GeV was also imposed, in order to reduce the contribution by nondiffractive events. The overall contamination integrated up to $|t| = 0.6$ GeV^2 was estimated to be $(23 \pm 8)\%$ for the BPC ρ^0 sample and $(24^{+9}_{-5})\%$ for the DIS ρ^0 sample, where the errors represent the total statistical and systematic uncertainties. In the DIS J/ψ analysis, the contamination was found to be $(21^{+10}_{-9})\%$, consistent with the values found in the BPC and DIS ρ^0 analyses.

Contamination from elastic production of ω and ϕ mesons in the ρ^0 analyses was estimated by Monte Carlo studies to be less than 2%. Contamination from ψ' production in the J/ψ analysis is $(4 \pm 1)\%$ [51]. The Bethe-Heitler contribution is approximately 15%; its size was estimated from the LPAIR Monte Carlo simulation [52].

The photon-dissociative background was studied with a sample of events generated using PYTHIA. The events which pass the selection criteria of the present ρ^0 analyses have a flat distribution in $M_{\pi\pi}$ up to about $M_{\pi\pi} \simeq 1.4$ GeV. If all events at $M_{\pi\pi} = 1.4$ GeV are ascribed to this process, a 3% upper limit on the contamination from photon dissociation is deduced. A similar result is obtained if an extra constant term is added to the Breit-Wigner function used for the mass fit.

A contamination of 1.5% from beam-gas events was deduced from event samples derived from unpaired electron and proton bunches, to which all the selection criteria described earlier were applied.

All subsequent results are shown after subtraction of the contributions from proton-dissociative and (for the J/ψ analysis) Bethe-Heitler events. The estimates of the other backgrounds were included in the systematic uncertainties.

7 Systematic uncertainties

The systematic uncertainties are dominated by the uncertainties in the acceptance, the proton-dissociative background and the number of ρ^0 or J/ψ signal events. Table 1

summarises the various contributions to the uncertainties in the integrated cross section for the three analyses.

In the following sections, whenever a result for a given quantity was obtained from a fit, it should be understood that the corresponding systematic uncertainty was determined by repeating the fit for each systematic check. The differences between the values of the quantity thus found and its nominal value were added in quadrature.

The trigger efficiency and its uncertainty were estimated, whenever possible, by using samples of events selected by independent triggers. The model dependence was investigated by comparing the acceptances obtained with various Monte Carlo generators, or with the same generator but with different input parameters. In particular, the sensitivity to the W and Q^2 dependences of the cross section in the generator were studied, as well as the sensitivity to R. Various electron finders were used to estimate the uncertainty due to the electron identification in the DIS analyses. In the BPC case a significant contribution originates from the uncertainty in the BPC alignment; its effect increases with decreasing Q^2. The sensitivity to the cuts mostly reflects the effect of the CTD-CAL-matching and track quality requirements.

The contribution due to the extraction of the number of signal events, reflecting the sensitivity to the mass fitting procedure, has been discussed previously [3] for the ρ^0 analyses. In the J/ψ analysis, this uncertainty is dominated by the sensitivity to the shape used for the subtraction of the nonresonant background.

The uncertainties in the luminosity, trigger efficiency, photon flux determination, ω, ϕ and ψ' backgrounds, photon dissociation (for ρ^0s), proton dissociation, beam-gas contamination, and J/ψ decay branching ratios are treated as overall normalisation uncertainties. In addition, for the BPC ρ^0 and J/ψ analyses, the contributions from the signal extraction procedure and from radiative corrections were included in the normalisation uncertainty. The normalisation uncertainties are $^{+9\%}_{-14\%}$ for DIS ρ^0, $^{+15\%}_{-16\%}$ for BPC ρ^0, and $^{+13\%}_{-15\%}$ for the J/ψ, dominated by proton dissociation and, for the BPC ρ^0, the signal extraction.

8 Results

8.1 Mass distributions

Acceptance-corrected differential distributions $\mathrm{d}N/\mathrm{d}M_{\pi^+\pi^-}$ for BPC and DIS ρ^0 samples are shown in Fig. 7. The $\pi^+\pi^-$ mass spectra deviate from the shape of a relativistic p-wave Breit-Wigner function. This effect may be explained by the interference between nonresonant and resonant $\pi^+\pi^-$ production amplitudes [53]. The differential distributions $\mathrm{d}N/\mathrm{d}M_{\pi^+\pi^-}$ were fitted in the range $0.6 < M_{\pi^+\pi^-} < 1.2$ GeV, in several Q^2 intervals, using a parameterisation based on the Söding model [53], which accounts for the effect of

interference according to [49]

$$\mathrm{d}N/\mathrm{d}M_{\pi\pi} = \left|A\frac{\sqrt{M_{\pi\pi}M_\rho\Gamma_\rho}}{M_{\pi\pi}^2 - M_\rho^2 + iM_\rho\Gamma_\rho} + B\right|^2, \tag{18}$$

where M_ρ and Γ_ρ are the nominal mass and width of the ρ^0 meson, respectively; B is the nonresonant amplitude assumed to be constant and real and A is a normalisation constant. The values of the ρ^0 meson mass and width obtained by fitting Eq. 18 are 768 ± 3(stat.) MeV and 152 ± 6(stat.) MeV for the BPC ρ^0 sample and 762 ± 3(stat.) MeV and 146 ± 7(stat.) MeV for the DIS ρ^0 sample. The ratio B/A decreases with Q^2, as shown in Fig. 7.

The uncorrected differential distribution $\mathrm{d}N/\mathrm{d}M_{\mathrm{l^+l^-}}$ for the DIS J/ψ sample, shown in Fig. 8, was fitted in the range $2 < M_{\mathrm{l^+l^-}} < 4$ GeV with the sum of a signal function and an exponentially falling background. The former is a convolution of a Gaussian resolution function with the J/ψ mass spectrum obtained using the DIPSI Monte Carlo generator [42] including bremsstrahlung. No positive muon or electron identification was performed; the muon mass was used in calculating $M_{\mathrm{l^+l^-}}$. The main contributions to the background are from oppositely charged hadrons and from the Bethe-Heitler process. The fitted value of the J/ψ mass is 3.114 ± 0.006(stat.) GeV and the width of the Gaussian resolution function is 26 MeV. Integrating the fitted function in the above $M_{\mathrm{l^+l^-}}$ range yields a signal of 97 ± 12 J/ψ mesons.

8.2 Total cross sections

The total cross sections for exclusive ρ^0 and J/ψ electroproduction, $\mathrm{ep} \to \mathrm{eVp}$, were determined using the expression

$$\sigma(\mathrm{ep} \to \mathrm{eVp}) = \frac{N \cdot \Delta}{A \cdot \mathcal{L}}, \tag{19}$$

where N is the number of events in data, A the overall acceptance, $\mathcal{L}$ the integrated luminosity and Δ the correction for the proton dissociation background. For the ρ^0 we quote the integrated cross sections for $|t| < 0.6$ GeV^2 and for the invariant mass range $2m_\pi < M_{\pi\pi} < M_\rho + 5\Gamma_\rho$, where m_π is the mass of a charged pion, $M_{\pi\pi}$ is the invariant mass of the two pions, M_ρ is the nominal ρ^0 mass and Γ_ρ is the width of the ρ^0 resonance at the nominal ρ^0 mass. In the DIS ρ^0 analysis, we correct to the Born level.

Total cross sections for exclusive ρ^0 and J/ψ production, $\mathrm{ep} \to \mathrm{eVp}$ and $\gamma^\star\mathrm{p} \to \mathrm{Vp}$, are given in Tables 2 and 3. The cross sections in each Q^2 and W interval are quoted at values close to the weighted averages in the bins. The $\gamma^\star$p cross sections were obtained from the ep cross sections using formulae (7)-(9). They are insensitive to the value of R since $\epsilon \simeq 1$.

8.3 Q^2 dependence

Fig. 9 shows the cross section for the process $\gamma^\star p \to \rho^0 p$ as a function of Q^2. The low-Q^2 data from this analysis have been fitted with two VMD-motivated functions and the corresponding curves are shown in the upper plot. A fit to the function $\sigma_{\rm tot}^{\gamma^\star {\rm p}} \propto [1+R(Q^2)]/(1+Q^2/M_{\rm eff}^2)^2$, yielded $M_{\rm eff} = 0.66 \pm 0.05({\rm stat.}) \pm 0.10({\rm syst.})$ GeV (here $R = \sigma_{\rm L}^{\gamma^\star {\rm p}}/\sigma_{\rm T}^{\gamma^\star {\rm p}}$ was taken as measured in this analysis). A fit to $\sigma_{\rm tot}^{\gamma^\star {\rm p}} \propto 1/(1+Q^2/M_\rho^2)^n$ gives $n = 1.75 \pm 0.10({\rm stat.}) \pm 0.29({\rm syst.})$ for the entire sample (W_0=50 GeV).

The $\gamma^\star$p cross sections are shown for the DIS data for fixed W as a function of Q^2 in the four lower plots. The cross section measurement at $Q^2 = 27(13)$ GeV^2 and $W = 80(120)$ GeV has been translated to $W = 70(110)$ GeV using the W dependence measured in this analysis. The data are consistent with a simple power law behaviour for $Q^2 > 5$ GeV^2. Fitting the points at $Q^2 > 5$ GeV^2 with the form Q^{-2n} yields $n = 2.07 \pm 0.22,\ 2.51 \pm 0.15,\ 2.15 \pm 0.31,\ 2.29 \pm 0.18$ for $W = 50, 70, 90, 110$ GeV, where the errors are statistical only. The systematic uncertainties are typically 0.05. The Q^2 dependence is consistent with being independent of W, and averaging the four values yields $n = 2.32 \pm 0.10({\rm stat.})$.

The data from this analysis are compared to previous HERA measurements in Fig. 10. The cross sections are quoted at the W values used by the H1 collaboration [15]. A comparison at fixed W entails smaller translation uncertainties than a comparison at fixed Q^2, as the W dependence is much weaker than the Q^2 dependence. A fit to the 95 ZEUS DIS data is shown to guide the eye. The results from this analysis are in excellent agreement with the previous ZEUS results [14]. The H1 data are systematically lower than the ZEUS measurements by approximately 30 to 40%.

A commonly adopted form for the Q^2 dependence of the J/ψ cross section is $\sigma_{\rm tot}^{\gamma^\star {\rm p}} \propto 1/(1+Q^2/M_{J/\psi}^2)^n$. This form was fitted to the $\gamma^\star {\rm p} \to J/\psi$ p cross section shown in Fig. 11. The curve on the figure represents this function fitted to the two measured data points (evaluated at W_0=90 GeV) yielding n=1.58$\pm$0.22(stat.)$\pm$0.09(syst.). This result is consistent with the H1 measurement of $n = 1.9 \pm 0.3({\rm stat.})$ [15].

8.4 W dependence

The measured cross section for exclusive ρ^0 production as a function of W for Q^2=0.47, 3.5, 7, 13 and 27 GeV^2 is presented in Fig. 12. The curves show the results of fits to the data using the function W^δ. The results of the fits are given in Table 4. The W dependence of the ρ^0 production cross section at low values of Q^2 (BPC ρ^0) rises slowly with W: δ=0.12$\pm$0.03(stat.)$\pm$0.08(syst.) for Q^2=0.47 GeV^2. This result is consistent with the value $\delta = 0.16 \pm 0.06({\rm stat.})^{+0.11}_{-0.15}({\rm syst.})$ measured in photoproduction [49]. Averaging the data in the range $3 < Q^2 < 20$ GeV^2 yields $\delta = 0.42 \pm 0.12({\rm stat.} \oplus {\rm syst.})$, which indicates that the W dependence increases with Q^2. In Fig. 13, the ZEUS data are compared to results from the NMC [12], E665 [13], and H1 [15] experiments. The NMC, E665 and H1 data points have been moved to coincide with the Q_0^2 values of the present analysis.

This was done according to the Q^2 dependence reported by each of the experiments. The H1 points at Q^2=13 GeV^2 were obtained by translating the cross sections measured at Q^2=10 GeV^2 and Q^2=20 GeV^2 and taking a weighted average. The NMC measurements were moved from Q^2=6.9 to Q^2=7.0 GeV^2 and from Q^2=11.9 to Q^2=13 GeV^2, using values of R from the model of Martin, Ryskin and Teubner [27] to evaluate $\sigma_{\rm T}^{\gamma^\star {\rm p}} + \sigma_{\rm L}^{\gamma^\star {\rm p}}$. The E665 measurements were moved from Q^2=0.61 to Q^2=0.47 GeV^2 and from Q^2=5.69 to Q^2=3.5 GeV^2.

The cross section for exclusive J/ψ photoproduction, measured at HERA and at low energies [54, 55], shows a rapid rise with W, approximately as $W^{0.8}$. The measured W dependence at higher values of Q^2 is also consistent with this behaviour, as can be seen in Fig. 14. In this figure, the H1 data points were scaled from Q^2=16 to 13 GeV^2. The curves, drawn to guide the eye, display a $W^{0.8}$ dependence.

8.5 Ratio of J/ψ and ρ^0 cross sections

The values of the ratio of J/ψ and ρ^0 ($\gamma^\star$p) cross sections, measured at Q^2=3.5 and 13 GeV^2, are given in Table 5. The correlated errors, which include those associated with the proton dissociation background subtraction, with the uncertainties in the trigger efficiency and with the uncertainty in the determination of the luminosity, do not contribute to the uncertainty in the ratio. The ratio increases with Q^2, as can be seen in Fig. 15.

8.6 Differential cross sections ${\rm d}\sigma^{\rm ep}/{\rm d}|t|$

The differential cross sections for exclusive ρ^0 production, ${\rm d}\sigma^{\rm ep}/{\rm d}|t|$, were measured in several Q^2 and W intervals; they are shown in Fig. 16 for the full data samples. The distributions were fitted with an exponential function of the form $\exp(-b|t|)$ for $|t| < 0.3$ GeV^2. Since a linear exponent is not sufficient to describe the data at higher $|t|$, the quadratic form $\exp(-b|t| + ct^2)$ was also fitted to both the BPC and DIS ρ^0 data for $|t| < 0.6$ GeV^2. The results from the linear fits are $b = 8.5 \pm 0.2({\rm stat.}) \pm 0.5({\rm syst.}) \pm 0.5({\rm pdiss.})$ GeV^{-2} for the BPC ρ^0 sample ($0.25 < Q^2 < 0.85$ GeV^2 and $20 < W < 90$ GeV) and $b = 8.1 \pm 0.6({\rm stat.}) \pm 0.7({\rm syst.}) \pm 0.7({\rm pdiss.})$ GeV^{-2} for the DIS ρ^0 sample, which covers the kinematic region depicted in Fig. 2. Since a major contribution to the systematic uncertainty arises from the uncertainty associated with subtracting the proton dissociation background, the error from this source is explicitly quoted. In order to illustrate the significance of the quadratic term in the exponent of the fitted function, the uncertainty due to the systematic error in the parameter c is indicated by a shaded band in Fig. 16. Detailed results of fits in Q^2, W and $M_{\pi\pi}$ intervals are summarised in Tables 6 and 7.

The slope parameter b as a function of W and Q^2 is displayed in Fig. 17. The results for BPC ρ^0 are consistent with a slow rise with W. The DIS ρ^0 results are consistent with no W dependence. Both results show significantly shallower slopes than that measured in photoproduction. The CDM calculation [20] is shown for comparison. Its prediction of a decrease with Q^2 is in reasonable agreement with the data.

The linear-exponent fit for the entire DIS J/ψ sample ($2 < Q^2 < 40$ GeV^2 and $55 < W < 125$ GeV) in the range $|t| < 1$ GeV^2 yielded $b = 5.1 \pm 1.1(\text{stat.}) \pm 0.7(\text{syst.})$ GeV^{-2}, a result consistent with the value of $4.6 \pm 0.4(\text{stat.})^{+0.4}_{-0.6}(\text{syst.})$ GeV^{-2} obtained in exclusive J/ψ photoproduction [10].

8.7 Shrinkage of the diffractive peak

Shrinkage of the diffractive peak was studied by reweighting iteratively the energy and b dependence in the Monte Carlo simulation according to

$$\frac{\mathrm{d}\sigma^{\mathrm{ep}}}{\mathrm{d}|t|} \propto \exp\left[(-b_0|t| + c_0 t^2) \cdot (W/W_0)^{4[(\alpha(0)-1)-\alpha'|t|]}\right], \qquad (20)$$

where W_0 is a constant, t and W are the generated variables, and b_0, $\alpha(0)$ and α' are the parameters tuned to the best agreement between the simulated and measured distributions. The fit for the BPC data yielded $\alpha(0)$=1.055$\pm$0.016(stat.)$\pm$0.019(syst.) and α'=0.19$\pm$0.09(stat.)$\pm$0.09(syst.) GeV^{-2}, showing evidence for shrinkage, in agreement with theoretical predictions [21]. A similar analysis performed using the DIS ρ^0 data gave an inconclusive result.

8.8 Decay angular distributions

The ρ^0 spin-density matrix elements, r^{04}_{00}, r^1_{1-1} and Re r^5_{10}, were determined by a two-dimensional maximum-likelihood fit of Eq. 12 to the $\cos\theta_{\mathrm{h}}$ and ψ_{h} distributions. The results are presented in Table 8. The corresponding values of the ratio $R = \sigma_{\mathrm{L}}^{\gamma^*\mathrm{p}}/\sigma_{\mathrm{T}}^{\gamma^*\mathrm{p}}$ as a function of Q^2 are displayed in the upper plot of Fig. 18. The ratio was evaluated according to Eq. 13. The results indicate that the ratio increases with Q^2, the Q^2 dependence steeper at lower Q^2. At high values of Q^2 the longitudinal cross section dominates. The solid line represents the result of a fit to the BPC data of the form $R = \kappa Q^2$, which yielded $\kappa = 0.81 \pm 0.05(\text{stat.}) \pm 0.06(\text{syst.})$. The dashed line represents the results of the QCD-based calculation of ref. [27], which describes the data well. The lower plots of Fig. 18 show R as a function of W for $Q^2 = 0.45$ GeV^2 and 6.2 GeV^2. For $Q^2 = 0.45$ GeV^2, the data indicate a slow decrease of R with W. However, they are consistent with no dependence within two standard deviations. For $Q^2 = 6.2$ GeV^2, the measurements indicate a slow rise of R with W. The prediction of the model of ref. [27] is in good agreement with these results.

The values of the spin-density matrix elements r^{04}_{00} and r^1_{1-1} satisfy Eq. 14 within experimental uncertainties, and are thus consistent with natural-parity exchange in the t channel.

The J/ψ spin-density matrix elements r^{04}_{00} and r^{04}_{1-1} were determined by one-dimensional fits of formulae (15) and (16). The results for the entire kinematic region covered by the data, for which $< Q^2 >= 5.9$ GeV^2 and $< W >= 97$ GeV, are

$$r^{04}_{00} = 0.29 \pm 0.19\,(\text{stat.})\,^{+0.12}_{-0.18}\,(\text{syst.}), \qquad r^{04}_{1-1} = -0.04 \pm 0.20\,(\text{stat.})\,^{+0.12}_{-0.22}\,(\text{syst.}).$$

Using $< \epsilon >= 0.99$, a value of R of $0.41^{+0.45}_{-0.52}$ (statistical and systematic uncertainties added in quadrature) was extracted, significantly less than the values measured for the ρ^0 at similar Q^2.

8.9 Forward longitudinal cross sections

In order to compare our results to pQCD calculations, we extract the forward longitudinal ρ^0 cross section according to

$$\left.\frac{\mathrm{d}\sigma_{\mathrm{L}}^{\gamma^\star \mathrm{p}}}{\mathrm{d}|t|}\right|_{t=0} = \left(\frac{R}{1+R}\right)\left(\frac{b}{1-e^{-b\,|t|_{\mathrm{max}}}}\right)\sigma_{\mathrm{tot}}^{\gamma^\star \mathrm{p}}, \qquad (21)$$

where $|t|_{\mathrm{max}}$ is the upper limit on $|t|$ for which the cross section was calculated. A comparison of the measured and the predicted x dependence of the longitudinal ρ^0 production cross section at various values of Q^2 is shown in Figs. 19-21. The shaded areas indicate normalisation uncertainties due to the proton dissociation background subtraction, the measured values of R and of the slope parameter b. (For the highest Q^2 value, extrapolations of the R and b values were used.)

In the model of Frankfurt, Koepf and Strikman [25] the hard diffractive production of vector mesons by longitudinal photons is calculated in the leading-order approximation ($\alpha_{\mathrm{s}} \ln \frac{Q^2}{\Lambda^2}$) using leading-order parton distributions. Rescaling effects are accounted for by introducing an effective scale, Q^2_{eff}, at which the gluon density is evaluated. The curves in Fig. 19, which use the ZEUS 94 next-to-leading-order (NLO) gluon density parameterisation [56], show the degree to which the rescaling attenuates the Q^2 dependence. Also shown are the effects of two assumptions concerning the ρ^0 wave function which result in different Fermi motion suppression factors as calculated by the authors. The assumption of a hard Fermi suppression attenuates the Q^2 dependence, as does the rescaling, but with a different x dependence. The two effects are of comparable magnitude in the kinematic region covered by the data. The measurements indicate that the assumption of a hard Fermi suppression together with the Q^2-rescaling results in an overcorrection. Clearly a quantitative understanding of the higher-order QCD corrections is necessary before information on the gluon density and on the ρ meson wave function can be extracted.

The model of Martin, Ryskin and Teubner [27] is based on the parton–hadron duality hypothesis, applied to the production of $\mathrm{q\bar{q}}$ pairs. A comparison of the predictions using various gluon density functions to the measured x dependence of the forward longitudinal cross section is shown in Fig. 20. The MRSA′ [43], MRSR2 [57], and ZEUS 94 NLO gluon density parameterisations lead to similar predictions, whereas the prediction using the GRV94 parameterisation [58] is considerably higher. In the context of this model, the data are sufficiently precise to distinguish between GRV94 and the other parton density functions.

Fig. 21 compares the calculations of the two models described above with that of Nemchik et al. [20], which is based on colour dipole BFKL phenomenology. Here, the model of

Frankfurt, Koepf, and Strikman uses the ZEUS 94 NLO gluon density function with rescaling and no hard Fermi suppression. The curves for the model of Martin, Ryskin, and Teubner represent a calculation which also employs the ZEUS 94 NLO gluon density parameterisation. With these choices, the models describe the data reasonably well, taking into account the normalisation uncertainties. Note that the normalisation uncertainty due to the uncertainty in b is largely independent for the various Q^2 values and dominates at high Q^2. The model of Nemchik et al. underestimates the cross section over the entire kinematic range investigated.

9 Summary and conclusions

We have studied the exclusive electroproduction of ρ^0, ep $\to$ eρ^0p, and J/ψ mesons, ep $\to$ eJ/ψ p, in the kinematic range $0.25 < Q^2 < 50$ GeV^2, $20 < W < 167$ GeV for the ρ^0 data and $2 < Q^2 < 40$ GeV^2, $50 < W < 150$ GeV for the J/ψ data. The results can be summarised as follows.

- The $\pi^+\pi^-$ mass spectrum for exclusively produced ρ^0 mesons shows a deviation from the relativistic p-wave Breit-Wigner shape. This can be explained in terms of the interference between resonant and nonresonant production amplitudes. The relative contribution of the nonresonant amplitude is found to decrease with Q^2 and becomes consistent with zero at $Q^2 \simeq 20$ GeV^2.

- The Q^2 dependence of the $\gamma^\star$p $\to \rho^0 p$ cross section at low Q^2 ($0.25 < Q^2 < 0.85$ GeV^2) can be described by the function $\sigma_{\rm tot}^{\gamma^\star {\rm p}} \propto 1/(1+Q^2/M_\rho^2)^n$ with $n = 1.75 \pm 0.10$ (stat.)$\pm$0.29(syst.). At higher values of Q^2 the dependence can be fitted with the function $\sigma_{\rm tot}^{\gamma^\star {\rm p}} \propto Q^{-2n}$ with the average fitted value of $n = 2.3 \pm 0.1$(stat.), essentially independent of W. For the DIS J/ψ sample the data are described by the function $\sigma_{\rm tot}^{\gamma^\star {\rm p}} \propto 1/(1+Q^2/M_{J/\psi}^2)^n$, with n=1.58$\pm$0.22(stat.)$\pm$0.09(syst.).

- The W dependence of the $\gamma^\star$p $\to \rho^0 p$ cross section exhibits a slow rise with W at low values of Q^2. Parameterising the cross section as $\sigma_{\rm tot}^{\gamma^\star {\rm p}} \propto W^\delta$ yields the fit result δ=0.12$\pm$0.03(stat.)$\pm$0.08(syst.) for Q^2=0.47 GeV^2 (BPC ρ^0). This value is consistent with that measured in photoproduction as well as with predictions based on soft pomeron exchange [8]. The slope becomes steeper with increasing Q^2. For $3.5 < Q^2 < 13$ GeV^2 the average value is 0.42 ± 0.12. This is less steep than the value of δ=0.92$\pm$0.14(stat.)$\pm$0.10(syst.) measured in J/ψ photoproduction [10]. The cross section for J/ψ electroproduction has a W dependence consistent with the steep dependence found in photoproduction.

- The ratio $\sigma(J/\psi)/\sigma(\rho^0)$ increases with Q^2 but does not reach the flavour-symmetric expectation of 8/9 at $Q^2 = 13$ GeV^2.

- The t distributions for exclusive ρ^0 production are well described by an exponential dependence ${\rm d}\sigma^{\rm ep}/{\rm d}|t| \propto e^{-b|t|}$ for $|t| < 0.3$ GeV^2 with $b \simeq 8$ GeV^{-2}. The slope

decreases at larger values of $|t|$. The Colour Dipole Model [20] gives a reasonable description of the data. A lower value, $5.1 \pm 1.1(\text{stat.}) \pm 0.7(\text{syst.})$ GeV^{-2}, has been obtained in exclusive J/ψ production in the kinematic region $2 < Q^2 < 40$ GeV^2 for $|t| < 1$ GeV^2. This result is compatible with that for J/ψ photoproduction.

- The ρ^0 measurements in the range $0.25 < Q^2 < 0.85$ GeV^2 exhibit a W dependence in the $|t|$ distribution. This may be interpreted as due to the shrinkage of the diffractive peak, predicted in Regge theory. In this context, we find $\alpha(0)=1.055\pm0.016(\text{stat.})\pm0.019(\text{syst.})$ and $\alpha'=0.19\pm0.09(\text{stat.})\pm0.09(\text{syst.})$ GeV^{-2}. Tests for shrinkage in the DIS ρ^0 sample were inconclusive.

- The ratio of the cross sections for longitudinal and transverse photons, $R = \sigma_{\text{L}}^{\gamma^\star \text{p}}/\sigma_{\text{T}}^{\gamma^\star \text{p}}$, increases with Q^2 and shows a weak W dependence. For $Q^2 > 3$ GeV^2 these dependences are well reproduced by the model of Martin, Ryskin and Teubner [27]. For J/ψ electroproduction, $R \simeq 0.4$ at $Q^2 = 6$ GeV^2, in contrast to the value of $R \gtrsim 2$ for the ρ^0 meson.

- The measurements of the forward longitudinal cross section, $\text{d}\sigma_{\text{L}}^{\gamma^\star \text{p}}/\text{d}|t||_{t=0}$, for ρ^0 production have been compared to the results of calculations based on several pQCD models. The present level of accuracy in the measurements allows quantitative distinctions between the various calculations.

In conclusion, our results for exclusive ρ^0 production show the Q^2 range $0.25 < Q^2 < 50$ GeV^2 to be a transition region, where, as Q^2 increases, the relative contribution of continuum $\pi^+\pi^-$ production decreases, and the longitudinal contribution to the total cross section increases and becomes dominant. These trends encourage efforts to describe this process using the methods of perturbative QCD.

Exclusive J/ψ electroproduction is consistent with expectations from pQCD. The exponential slope of the $|t|$ dependence is approximately 5 GeV^{-2} and the W dependence of the cross section is consistent with the steep rise observed in J/ψ photoproduction. These dependences differ from those measured in ρ^0 electroproduction at $Q^2 \simeq M_{J/\psi}^2$, where the $|t|$ dependence is steeper and the W dependence shallower. We also find contrasting values for R in J/ψ and ρ^0 electroproduction. Thus Q^2 and M_{V}^2 are shown to play dissimilar roles in setting the scale of the process.

Acknowledgements

We thank the DESY Directorate for their strong support and encouragement, and the HERA machine group for their diligent efforts. We are grateful for the support of the DESY computing and network services. The design, construction and installation of the ZEUS detector have been made possible owing to the ingenuity and effort of many people from DESY and home institutes who are not listed as authors. It is also a pleasure to thank L. Frankfurt, W. Koepf, A.D. Martin, J. Nemchik, N.N. Nikolaev, M.G. Ryskin,

M. Strikman and T. Teubner for many useful discussions and for providing model calculations.

References

[1] J.A. Crittenden, *Exclusive Production of Neutral Vector Mesons at the Electron-Proton Collider HERA,* Springer Tracts in Modern Physics, Volume 140 (Springer, Berlin Heidelberg, 1997).

[2] R.M. Egloff et al., Phys. Rev. Lett. 43 (1979) 657;
R.M. Egloff et al., Phys. Rev. Lett. 43 (1979) 1545;
D. Aston et al., Nucl. Phys. B209 (1982) 56;
J. Busenitz et al., Phys. Rev. D40 (1989) 1.
For a review of earlier results, see T.H. Bauer, R.D. Spital, D.R. Yennie and F.M. Pipkin, Rev. Mod. Phys. 50 (1978) 261; Erratum ibid. 51 (1979) 407; and references therein.

[3] ZEUS Collab., M. Derrick et al., Z.Phys. C69 (1995) 39.

[4] ZEUS Collab., M.Derrick et al., Phys. Lett. B377 (1996) 259.

[5] ZEUS Collab., M.Derrick et al., Z. Phys. C73 (1996) 73;
H1 Collab., S. Aid et al., Nucl. Phys. B463 (1996) 3;
ZEUS Collab., M.Derrick et al., Z. Phys. C73 (1997) 253.

[6] see e.g. P.D.B. Collins, *Introduction to Regge Theory and High Energy Physics* (Cambridge University Press, 1977).

[7] J.J. Sakurai, *Currents and Mesons* (University of Chicago Press, 1969);
H. Fraas and D. Schildknecht, Nucl. Phys., B14 (1969) 543.

[8] A. Donnachie and P.V. Landshoff, Phys. Lett. B296 (1992) 227.

[9] ZEUS Collab., M.Derrick et al., Phys. Lett. B350 (1995) 120;
H1 Collab., S. Aid et al., Nucl. Phys., B472 (1996) 3.

[10] ZEUS Collab., J. Breitweg et al., Z. Phys. C75 (1997) 215.

[11] EMC Collab., J.J. Aubert et al., Phys. Lett. B161 (1985) 203.

[12] NMC Collab., M. Arneodo et al., Nucl. Phys. B429 (1994) 503.

[13] E665 Collab., M.R. Adams et al., Z.Phys. C74 (1997) 237.

[14] ZEUS Collab., M. Derrick et al., Phys. Lett. B356 (1995) 601;
ZEUS Collab., M. Derrick et al., Phys. Lett. B380 (1996) 220.

[15] H1 Collab., S. Aid et al., Nucl.Phys. B468 (1996) 3;
Erratum in preparation for Nucl.Phys. B.

[16] S.J. Brodsky et al., Phys. Rev. D50 (1994) 3134.

[17] M.G. Ryskin, Z. Phys. C57 (1993) 89.

[18] ZEUS Collab., M. Derrick et al., Phys. Lett. B345 (1995) 576;
H1 Collab., S. Aid et al., Nucl. Phys., B470 (1996) 3.

[19] M.G. Ryskin, R.G. Roberts, A.D. Martin and E.M. Levin, Z. Phys. C76 (1997) 231.

[20] J. Nemchik, N.N. Nikolaev and B.G. Zakharov, Phys. Lett. B341 (1994) 228;
J. Nemchik, N.N. Nikolaev, E. Predazzi and B.G. Zakharov,
Phys. Lett. B374 (1996) 199;
J. Nemchik, N.N. Nikolaev, E. Predazzi and B.G. Zakharov, Z. Phys. C75 (1997) 71;
J. Nemchik et al., LANL Preprint HEP–PH/97-12-469 (1997).

[21] A. Donnachie and P.V. Landshoff, Phys. Lett. B348 (1995) 213;
J.R. Cudell and I. Royen, Phys. Lett. B397 (1997) 317.

[22] I.F. Ginzburg and D.Yu. Ivanov, Phys. Rev. D54 (1996) 5523;
D.Yu. Ivanov, Phys. Rev. D53 (1996) 3564.

[23] J.C. Collins, L. Frankfurt and M. Strikman, Phys. Rev. D56 (1997) 2982.

[24] CTEQ Collab., H.L. Lai et al., Phys. Rev. D51 (1995) 4763.

[25] L. Frankfurt, W. Koepf and M. Strikman, Phys. Rev. D54 (1996) 3194.

[26] L. Frankfurt and M. Strikman, LANL Preprint HEP–PH/95-10-291 (1997).

[27] A.D. Martin, M.G. Ryskin and T. Teubner, Phys. Rev. D55 (1997) 4329.

[28] The ZEUS Detector, Status Report, DESY (1993).

[29] M. Derrick et al., Nucl. Instrum. Methods A309 (1991) 77;
A. Andresen et al., Nucl. Instrum. Methods A309 (1991) 101;
A. Bernstein et al., Nucl. Instrum. Methods A336 (1993) 23.

[30] N. Harnew et al., Nucl. Instrum. Methods A279 (1989) 290;
B. Foster et al., Nucl. Phys. B, Proc-Suppl. B32 (1993) 181;
B. Foster et al., Nucl. Instrum. Methods, A338 (1994) 254.

[31] D. Kisielewska et al., DESY-HERA 85-25 (1985);
J. Andruszków et al., DESY 92-066 (1992).

[32] L.N. Hand, Phys. Rev. 129 (1963) 1834.

[33] K. Schilling and G. Wolf, Nucl. Phys. B61 (1973) 381.

[34] J. Ballam et al., Phys. Rev. D5 (1972) 545;
P. Joos et al., Nucl. Phys. B113 (1976) 53;
F.J. Gilman, J. Pumplin, A. Schwimmer and L. Stodolsky, Phys. Lett. B31 (1970) 387.

[35] W.H. Smith et al., Nucl. Instrum. Methods A355 (1995) 278.

[36] H. Abramowicz, A. Caldwell and R. Sinkus, Nucl. Instrum. Methods A365 (1995) 508;
R. Sinkus, Ph.D. thesis, Hamburg University (1996).

[37] T. Monteiro, Ph.D. thesis, Hamburg University (1998).

[38] H. Beier, Ph.D. thesis, Hamburg University (1997).

[39] T. Sjöstrand, Comp. Phys. Commun. 39 (1986) 347;
T. Sjöstrand and M. Bengtsson, Comp. Phys. Commun. 43 (1987) 367.

[40] A. Kwiatkowski, H. Spiesberger and H.-J. Moehring, in *Proceedings of the Workshop on Physics at HERA, Volume III*, edited by W. Buchmüller and G. Ingelman (DESY, Hamburg, Germany, 1991), p. 1294.

[41] K. Muchorowski, Ph.D. thesis, Warsaw University (1998).

[42] M. Arneodo, L. Lamberti and M.G. Ryskin, Comp. Phys. Commun. 100 (1997) 195.

[43] A.D. Martin, W.J. Stirling and R.G. Roberts, Phys. Lett. B354 (1995) 155.

[44] M. Kasprzak, Ph.D. thesis, Warsaw University (1996).

[45] G. Marchesini et al., Comp. Phys. Commun. 67 (1992) 465;
B.R. Webber, in *Proceedings of the Workshop on Physics at HERA, Volume III*, edited by W. Buchmüller and G. Ingelman (DESY, Hamburg, Germany, 1991), p. 1354;
L. Stanco, ibid., p. 1363.

[46] T. Sjöstrand, Z. Phys. C42 (1989) 301.

[47] CDF Collab., F. Abe et al., Phys. Rev. D50 (1994) 5535.

[48] For reviews, see e.g.
G. Alberi and G. Goggi, Phys. Rep. 74 (1981) 1;
K. Goulianos, Phys. Rep. 101 (1983) 169;
N.P. Zotov and V.A. Tsarev, Sov. Phys. Uspekhi 31 (1988) 119;
G. Giacomelli, Int. J. Mod. Phys. A, Volume 5 (1990) 223.

[49] ZEUS Collab., J. Breitweg et al., E. Phys. J. C2 (1998) 247.

[50] H1 Collab., C. Adloff et al., Z. Phys. C75 (1997) 607.

[51] S. Wang, Ph.D. thesis, University of Iowa (1998).

[52] J.A.M. Vermaseren, Nucl. Phys. B229 (1983) 347; S.P. Baranov, O. Dünger, H. Shooshtari, and J.A.M. Vermaseren, in *Proceedings of the Workshop on Physics at HERA, Volume III*, edited by W. Buchmüller and G. Ingelman (DESY, Hamburg, Germany, 1991), p. 1478.

[53] P. Söding, Phys. Lett. 19 (1966) 702.

[54] E401 Collab., M. Binkley et al., Phys. Rev. Lett. 48 (1982) 73.

[55] E516 Collab., B.H. Denby et al., Phys. Rev. Lett. 52 (1984) 795.

[56] ZEUS Collab., M. Derrick et al., Z. Phys. C72 (1996) 399.

[57] A.D. Martin, R.G. Roberts and W.J. Stirling, Phys. Lett. B387 (1996) 419.

[58] M. Glück, E. Reya and A. Vogt, Z. Phys. C67 (1995) 433.

Contribution from	BPC ρ^0	DIS ρ^0	DIS J/ψ
Luminosity	1.1*	1.1*	1.1*
Acceptance: trigger efficiency	5.5*	<1*	<1*
Acceptance: model dependence	1-4	5*	1
Acceptance: electron identification	3-10	<1	<1
Acceptance: dependence on cuts	2-10	6	$^{+6}_{-11}$
Acceptance: photon flux determination	1*	1	1*
Procedure to extract the signal events	10*	1*	5*
Proton diss. background subtraction	10*	$^{+7}_{-12}$ *	$^{+11}_{-13}$*
Elastic ω and ϕ production	1.6*	<1*	–
Elastic ψ' production	–	–	1*
Photon diffractive dissociation	$^{+0}_{-3}$*	$^{+0}_{-3}$*	–
Radiative corrections	2*	1*	4*
Beam-gas interactions	$^{+0}_{-1.5}$ *	$^{+0}_{-1.5}$ *	$^{+0}_{-1.5}$ *
Branching ratio	–	–	2.2*

Table 1: Typical values of relative contributions (%) to the systematic uncertainty in the integrated cross sections presented in Tables 2 and 3. The starred values are the contributions to the overall normalisation uncertainty in each of the three analyses.

W [GeV]	Q^2 [GeV^2]	#evts	W_0 [GeV]	Q_0^2 [GeV^2]	σ^{ep} [nb]	$\sigma^{\gamma^*\mathrm{p}}$ [μb]
BPC ρ^0						
	0.25-0.29	1074		0.27	4.99±0.15±0.47	5.07±0.15±0.48
	0.29-0.33	941		0.31	3.98±0.14±0.47	4.64±0.16±0.55
20-90	0.33-0.38	857	51.1	0.35	3.88±0.13±0.33	4.14±0.14±0.36
	0.38-0.45	869		0.41	4.34±0.15±0.56	3.86±0.13±0.49
	0.45-0.55	784		0.50	4.55±0.16±0.49	3.41±0.12±0.37
	0.55-0.85	937		0.69	7.28±0.23±1.06	2.51±0.08±0.37
20-27		955	23.4		5.52±0.18±0.64	3.16±0.10±0.37
27-35		1024	30.9		4.75±0.15±0.59	3.16±0.10±0.40
35-45	0.25-0.85	994	39.9	0.47	4.62±0.24±0.61	3.19±0.16±0.43
45-55		897	49.9		4.28±0.15±0.56	3.74±0.13±0.48
55-70		1018	62.4		4.89±0.15±0.50	3.61±0.11±0.38
70-90		574	79.8		4.72±0.20±0.56	3.44±0.14±0.40
DIS ρ^0						
32–40	3–5	254	36	3.5	$0.141 \pm 0.011^{+0.009}_{-0.010}$	$0.310 \pm 0.025^{+0.019}_{-0.022}$
40–60		492	50		$0.256 \pm 0.017^{+0.014}_{-0.014}$	$0.318 \pm 0.021^{+0.017}_{-0.017}$
60–80		401	70		$0.211 \pm 0.016^{+0.011}_{-0.014}$	$0.376 \pm 0.027^{+0.019}_{-0.025}$
80–100		318	90		$0.186 \pm 0.016^{+0.006}_{-0.014}$	$0.443 \pm 0.036^{+0.014}_{-0.025}$
40–60	5–10	380	50	7	$0.101 \pm 0.007^{+0.006}_{-0.006}$	$0.075 \pm 0.005^{+0.004}_{-0.005}$
60–80		331	70		$0.089 \pm 0.008^{+0.004}_{-0.004}$	$0.095 \pm 0.009^{+0.005}_{-0.005}$
80–100		234	90		$0.066 \pm 0.007^{+0.005}_{-0.007}$	$0.094 \pm 0.010^{+0.007}_{-0.010}$
100–120		193	110		$0.058 \pm 0.006^{+0.001}_{-0.002}$	$0.109 \pm 0.012^{+0.002}_{-0.004}$
41–60	10–20	106	50	13	$0.023 \pm 0.002^{+0.001}_{-0.002}$	$0.021 \pm 0.002^{+0.001}_{-0.002}$
60–80		88	70		$0.019 \pm 0.002^{+0.002}_{-0.002}$	$0.024 \pm 0.003^{+0.002}_{-0.002}$
80–100		72	90		$0.014 \pm 0.002^{+0.001}_{-0.002}$	$0.025 \pm 0.004^{+0.001}_{-0.002}$
100–140		110	120		$0.025 \pm 0.003^{+0.001}_{-0.003}$	$0.030 \pm 0.004^{+0.001}_{-0.003}$
55–96	20–50	27	80	27	$0.006 \pm 0.001^{+0.001}_{-0.001}$	$0.0033 \pm 0.0007^{+0.0004}_{-0.0004}$
96–125		17	110		$0.004 \pm 0.001^{+0.001}_{-0.002}$	$0.0045 \pm 0.0012^{+0.0010}_{-0.0018}$
125–167		16	150		$0.004 \pm 0.001^{+0.001}_{-0.001}$	$0.0053 \pm 0.0015^{+0.0017}_{-0.0010}$

Table 2: Exclusive ρ^0 production cross sections for $|t| < 0.6$ GeV^2 in various Q^2 and W intervals. The BPC ρ^0 cross sections are calculated for the invariant mass range $2m_\pi < M_{\pi\pi} < M_\rho + 5\Gamma_\rho$. The cross sections are given at Q_0^2 and W_0 values assuming the Q^2 and W dependence from this analysis. The uncertainties do not include the normalisation uncertainties, which are $^{+9\%}_{-14\%}$ for the DIS ρ^0 sample and, $^{+15\%}_{-16\%}$ for the BPC ρ^0 sample.

W [GeV]	Q^2 [GeV^2]	# events	W_0 [GeV]	Q_0^2 [GeV^2]	$\sigma^{\rm ep}$ [pb]	$\sigma^{\gamma^\star {\rm p}}$ [nb]
50–100	2–7	31±7	70	3.5	$79 \pm 18^{+11}_{-12}$	$21 \pm 5 \pm 3$
100–150	2–7	20±7	120	3.5	$56 \pm 19^{+10}_{-11}$	$29 \pm 10 \pm 6$
50–150	2–7		90	3.5	$135 \pm 26^{+18}_{-20}$	$25 \pm 5 \pm 4$
50–100	7–40	24±6	70	13.0	$30 \pm 7^{+4}_{-5}$	$6 \pm 2 \pm 1$
100–150	7–40	29±7	120	13.0	$39 \pm 9^{+5}_{-6}$	$17 \pm 4 \pm 3$
50–150	7–40		90	13.0	$69 \pm 12^{+8}_{-10}$	$10 \pm 2 \pm 2$

Table 3: Exclusive J/ψ production cross sections in various Q^2 and W intervals. Values are quoted at Q_0^2 and W_0. The first error is statistical, the second systematic. The systematic uncertainties include the normalisation uncertainty of $^{+13\%}_{-15\%}$ added in quadrature.

Q_0^2 [GeV^2]	δ
0.47	$0.12 \pm 0.03 \pm 0.08$
3.5	$0.40 \pm 0.12 \pm 0.12$
7.0	$0.45 \pm 0.15 \pm 0.07$
13.0	$0.41 \pm 0.19 \pm 0.10$
27.0	$0.76 \pm 0.55 \pm 0.60$

Table 4: The values of the parameter δ obtained by fitting the W dependence of $\sigma_{\rm tot}^{\gamma^\star {\rm p}}$ for exclusive ρ^0 production with a function $\sigma_{\rm tot}^{\gamma^\star {\rm p}} \propto W^\delta$. The first error is statistical, the second systematic.

Q_0^2 [GeV^2]	W_0 [GeV]	$\sigma(J/\psi)/\sigma(\rho^0)$
3.5	90	$0.06 \pm 0.01 \pm 0.01$
13.0	90	$0.43 \pm 0.10^{+0.03}_{-0.06}$

Table 5: The ratio of J/ψ and ρ^0 cross sections measured at two Q^2 values. The first error is statistical, the second systematic.

W_0 [GeV]	Q_0^2 [GeV^2]	$M_{\pi\pi}$ [GeV]	b [GeV^{-2}]
BPC ρ^0			
47	0.45	$0.6 < M_{\pi\pi} < 1.2$	$8.5 \pm 0.2 \pm 0.5 \pm 0.5$
25			$7.6 \pm 0.6 \pm 0.8 \pm 0.5$
35			$8.8 \pm 0.8 \pm 1.2 \pm 0.5$
50			$8.8 \pm 0.5 \pm 0.4 \pm 0.4$
74			$9.0 \pm 0.6 \pm 0.7 \pm 0.7$
47	0.33		$8.6 \pm 0.4 \pm 0.6 \pm 0.5$
47	0.62		$8.3 \pm 0.6 \pm 0.9 \pm 0.5$
47	0.45	$0.6 < M_{\pi\pi} < 0.7$	$9.7 \pm 0.7 \pm 0.8 \pm 0.5$
47		$0.7 < M_{\pi\pi} < 0.8$	$8.5 \pm 0.5 \pm 0.6 \pm 0.5$
47		$0.8 < M_{\pi\pi} < 1.2$	$7.8 \pm 0.6 \pm 0.6 \pm 0.5$
DIS ρ^0			
67	6.2	$0.6 < M_{\pi\pi} < 1.2$	$8.1^{+0.6+0.3+0.7}_{-0.6-0.7-0.4}$
50	6.2		$8.2^{+0.9\ +0.4+0.7}_{-0.9\ -0.4-0.4}$
70	6.2		$8.4^{+1.1\ +0.3+0.7}_{-1.1\ -0.8-0.4}$
90	6.2		$7.4^{+1.1\ +0.2+0.6}_{-1.0\ -0.9-0.3}$
67	3.8		$7.4^{+0.8\ +0.1+0.7}_{-0.8\ -1.0-0.3}$
67	6.8		$8.6^{+1.0\ +0.4+0.7}_{-0.9\ -0.6-0.4}$
67	13		$8.7^{+2.0\ +0.5+0.6}_{-1.8\ -1.3-0.3}$
102	28		$4.4^{+3.5\ +3.7+0.5}_{-2.8\ -1.2-0.3}$
67	6.2	$0.6 < M_{\pi\pi} < 0.8$	$8.3^{+0.8+0.2\ +0.8}_{-0.7-0.5\ -0.4}$
67	6.2	$0.8 < M_{\pi\pi} < 1.2$	$7.7^{+1.0+0.7\ +0.6}_{-0.9-1.1\ -0.3}$

Table 6: The values of the slope parameter b obtained by fitting $\mathrm{d}\sigma^{\mathrm{ep}}/\mathrm{d}|t| \propto e^{-b|t|}$ in the range $|t| < 0.3$ GeV^2 in various Q^2, W, and $M_{\pi^+\pi^-}$ ranges of the BPC and DIS ρ^0 samples. The first line of each of the BPC and DIS sections indicates the results of the fit to the full sample. The first error is statistical, the second systematic and the third is the uncertainty resulting from the subtraction of the proton dissociation background.

W_0 [GeV]	Q_0^2 [GeV^2]	b [GeV^{-2}]	c [GeV^{-4}]
47	0.45	$9.5 \pm 0.3 \pm 0.6 \pm 0.5$	$4.0 \pm 0.7 \pm 0.8 \pm 0.4$
67	6.2	$9.5 \pm 0.8 \pm 1.1 \pm 0.9$	$6.1 \pm 1.3 \pm 1.7 \pm 0.5$

Table 7: The values of the parameters b and c obtained by fitting $\sigma^{\rm ep}/{\rm d}|t| \propto e^{-b|t|+ct^2}$ in the range $|t| < 0.6$ GeV^2 for the full BPC and DIS ρ^0 samples. The mass range $0.6 < M_{\pi^+\pi^-} < 1.2$ GeV was used. The first error is statistical, the second systematic and the third is the uncertainty resulting from the subtraction of the proton dissociation background.

W_0 [GeV]	Q_0^2 [GeV^2]	r_{00}^{04}
27.5	0.45	$0.30 \pm 0.02 \pm 0.03$
45	0.45	$0.26 \pm 0.02 \pm 0.02$
71	0.45	$0.23 \pm 0.02 \pm 0.02$
47	0.33	$0.23 \pm 0.01 \pm 0.02$
47	0.62	$0.32 \pm 0.01 \pm 0.02$
46	6.2	$0.71 \pm 0.02 \pm 0.03$
67	6.2	$0.68 \pm 0.02 \pm 0.04$
92	6.2	$0.75 \pm 0.03 \pm 0.03$
67	3.8	$0.68 \pm 0.02 \pm 0.02$
67	6.8	$0.74 \pm 0.02 \pm 0.04$
67	14.1	$0.76 \pm 0.03 \pm 0.06$
W_0 [GeV]	Q_0^2 [GeV^2]	r_{1-1}^{1}
27.5	0.45	$0.32 \pm 0.01 \pm 0.03$
45	0.45	$0.35 \pm 0.01 \pm 0.02$
71	0.45	$0.36 \pm 0.01 \pm 0.02$
47	0.33	$0.36 \pm 0.01 \pm 0.02$
47	0.62	$0.31 \pm 0.01 \pm 0.03$
46	6.2	$0.12 \pm 0.02 \pm 0.02$
67	6.2	$0.15 \pm 0.02 \pm 0.06$
92	6.2	$0.10 \pm 0.02 \pm 0.04$
67	3.8	$0.15 \pm 0.02 \pm 0.02$
67	6.8	$0.11 \pm 0.02 \pm 0.02$
67	14.1	$0.08 \pm 0.03 \pm 0.07$
W_0 [GeV]	Q_0^2 [GeV^2]	Re r_{10}^{5}
27.5	0.45	$0.150 \pm 0.005 \pm 0.010$
45	0.45	$0.136 \pm 0.004 \pm 0.010$
71	0.45	$0.132 \pm 0.005 \pm 0.010$
47	0.33	$0.133 \pm 0.004 \pm 0.010$
47	0.62	$0.156 \pm 0.004 \pm 0.010$
46	6.2	$0.10 \pm 0.02 \pm 0.03$
67	6.2	$0.11 \pm 0.02 \pm 0.03$
92	6.2	$0.11 \pm 0.02 \pm 0.03$
67	3.8	$0.11 \pm 0.02 \pm 0.04$
67	6.8	$0.10 \pm 0.02 \pm 0.03$
67	14.1	$0.09 \pm 0.03 \pm 0.03$

Table 8: The spin-density matrix elements r_{00}^{04}, r_{1-1}^{1} and Re r_{10}^{5} determined using Eq. 12 for various values of W and Q^2 (BPC and DIS ρ^0 samples). The first error is statistical, the second systematic.

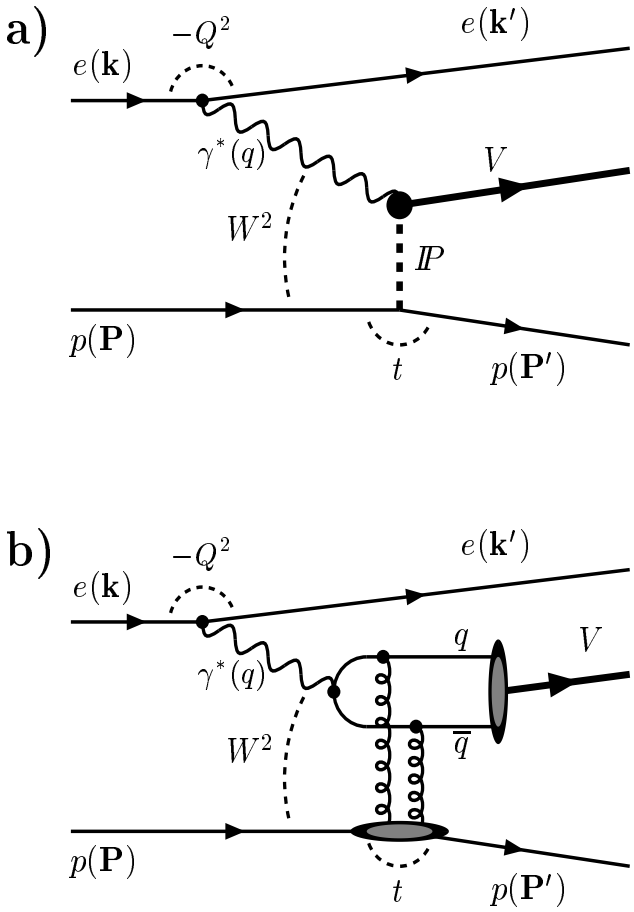

Figure 1: Diagrams illustrating the exclusive electroproduction of vector mesons a) via pomeron exchange, and b) via exchange of a gluon pair.

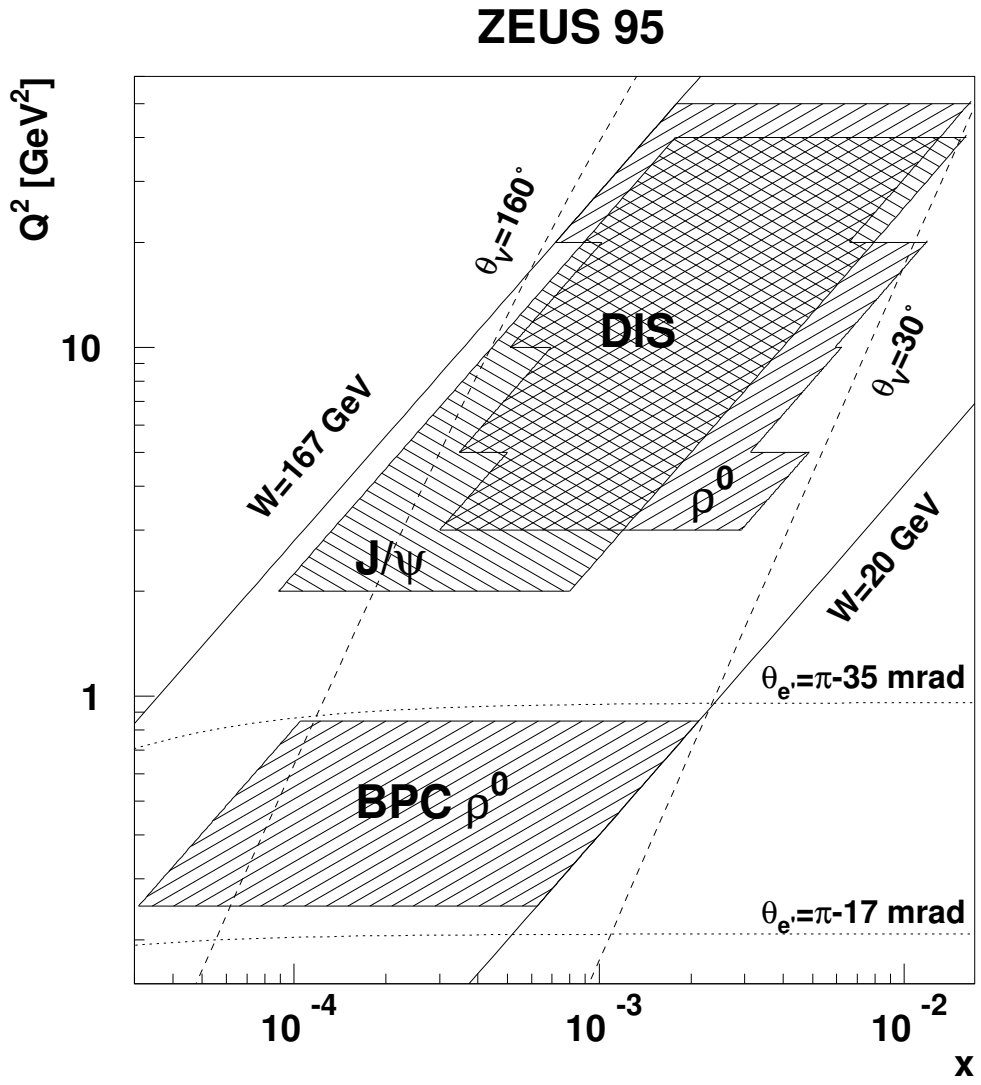

Figure 2: The kinematic regions covered by the ρ^0 and J/ψ data samples used for this analysis. Line types: solid – constant W; dashed – constant polar scattering angle of the vector meson ($\theta_{\rm V}$); and, dotted – constant positron scattering angle ($\theta_{e'}$).

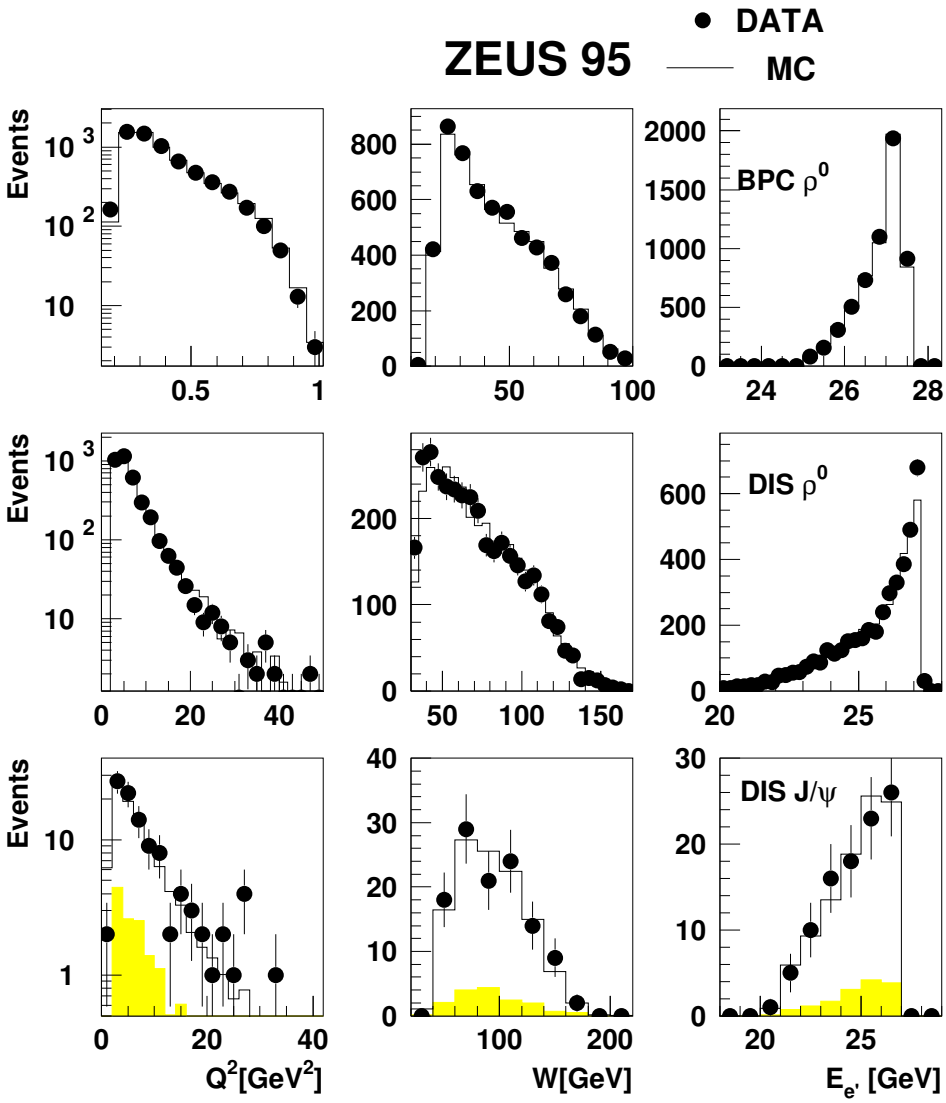

Figure 3: Comparison of the measured and Monte-Carlo-simulated distributions for Q^2, W and $E_{e'}$, the energy of the scattered positron. The shaded area indicates the contribution from the Bethe-Heitler process.

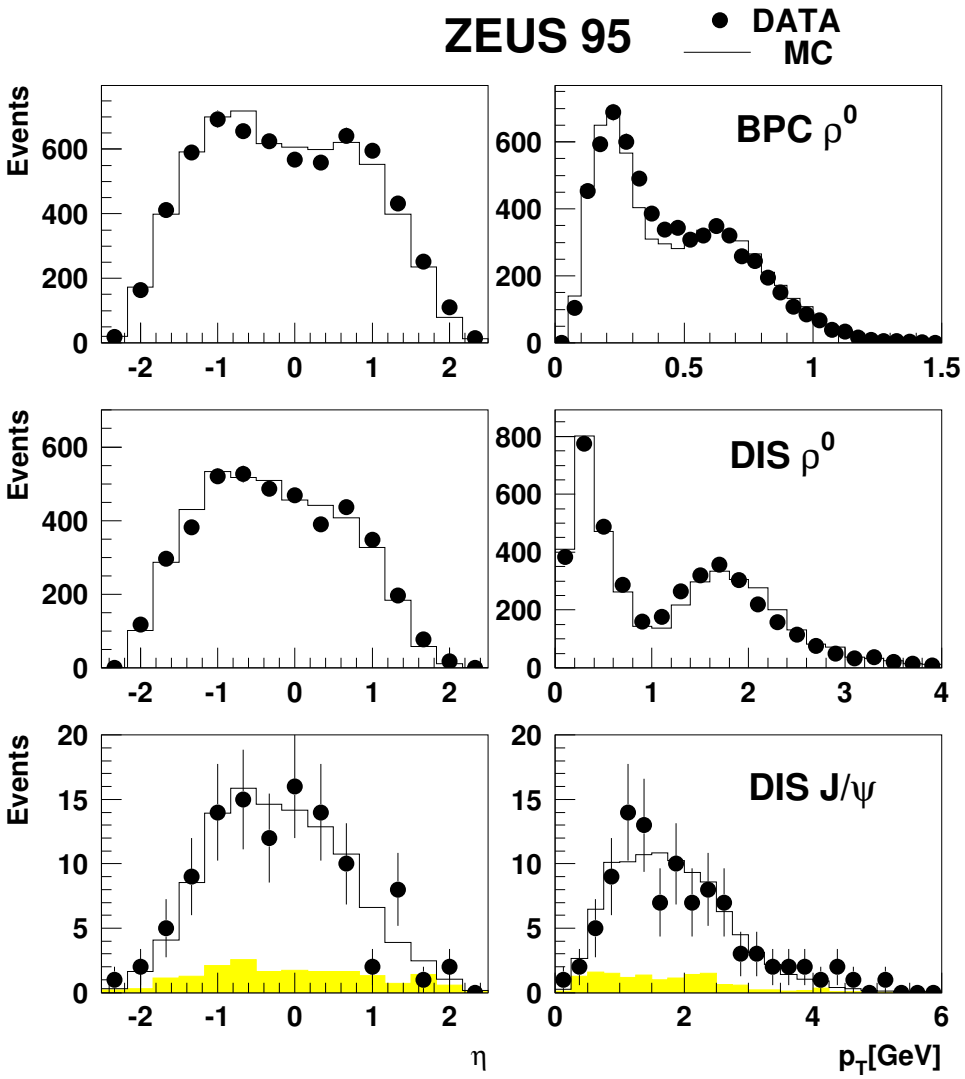

Figure 4: Comparison of the measured and Monte-Carlo-simulated distributions for pseudorapidity, η, and the transverse momentum in the laboratory frame, p_{T}, for the positively charged decay particle. The shaded area indicates the contribution from the Bethe-Heitler process.

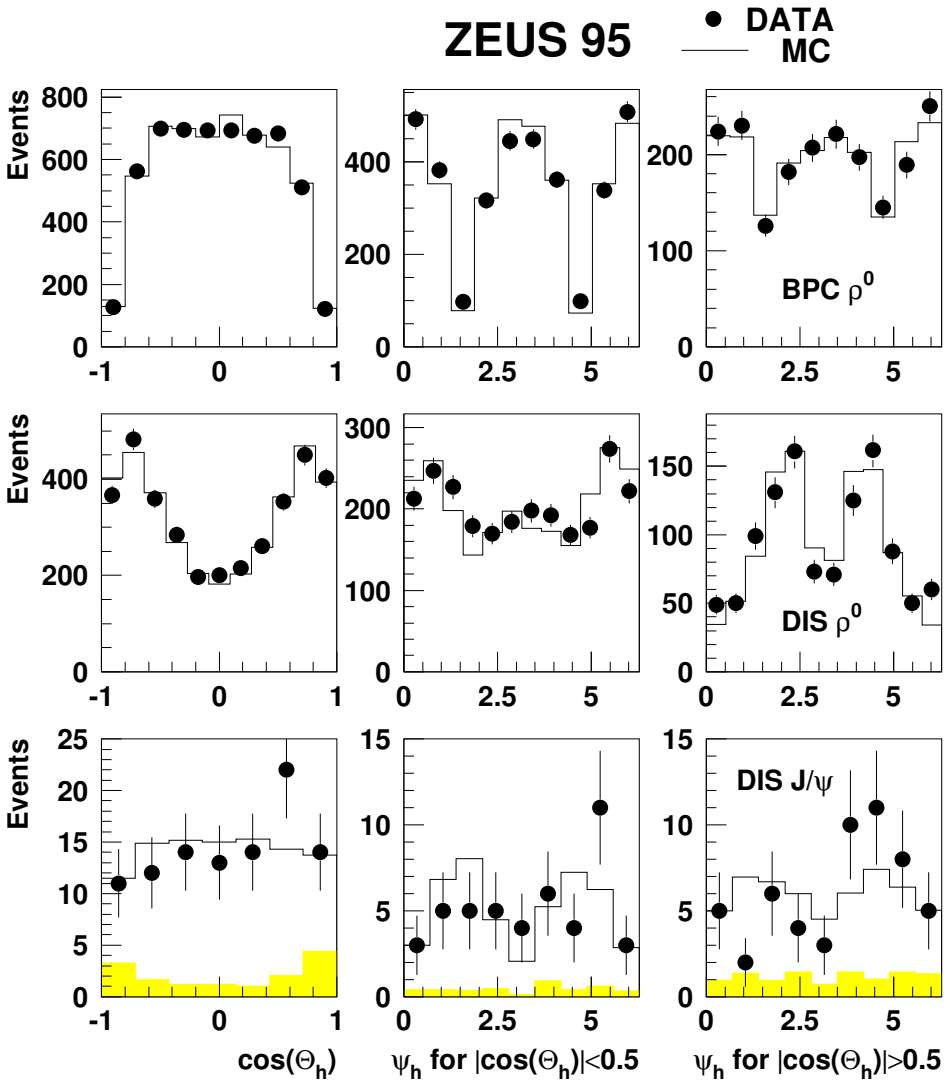

Figure 5: Comparison of the measured and Monte-Carlo-simulated distributions of $\cos\theta_{\rm h}$ and $\psi_{\rm h}$. The $\psi_{\rm h}$ distributions are shown for two ranges of $\cos\theta_{\rm h}$. The strong correlation of these variables is evident. The shaded area indicates the contribution from the Bethe-Heitler process.

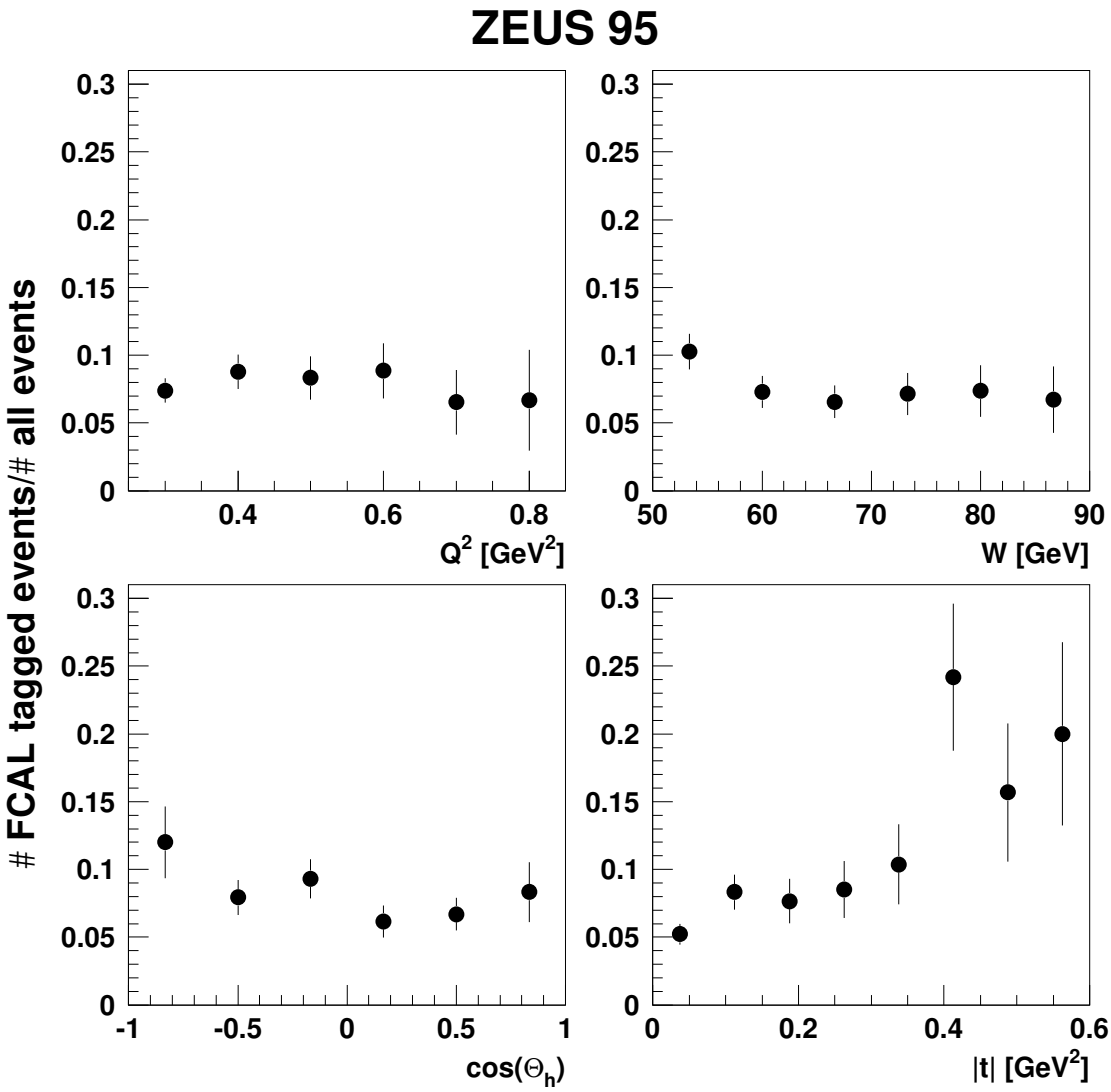

Figure 6: The fraction of events tagged with the FCAL as a function of Q^2, W, $\cos\theta_{\rm h}$ and $|t|$ for the BPC ρ^0 sample.

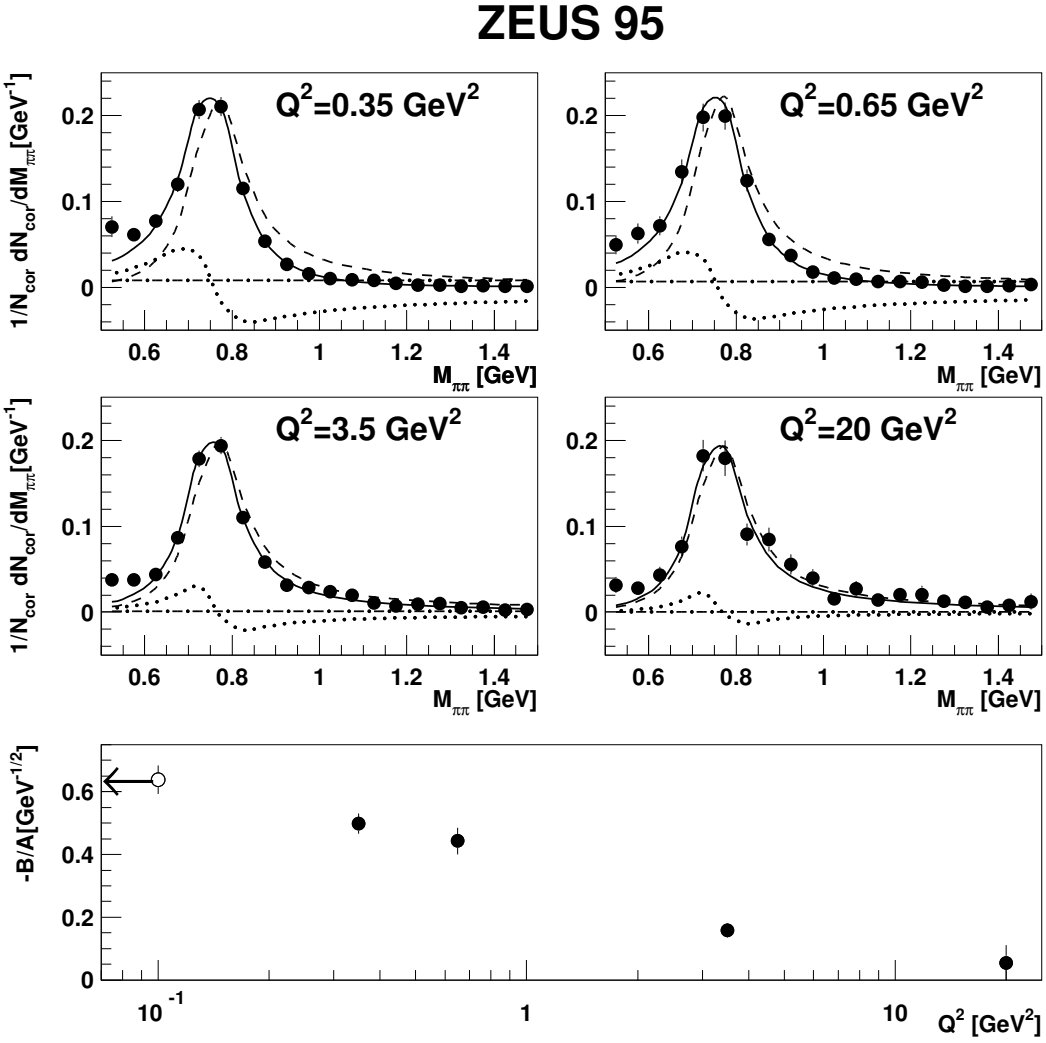

Figure 7: Top: The acceptance-corrected differential mass distributions, normalised to unit area, for the BPC and DIS ρ^0 samples. Line types: solid – fit based on the Söding model [53](cf. Eq. 18); dashed – contribution from the p-wave Breit-Wigner term; dotted – interference term; dash-dotted – background contribution. Bottom: ratio B/A (cf. Eq. 18). The open point associated with an arrow indicates the value measured in photoproduction [49].

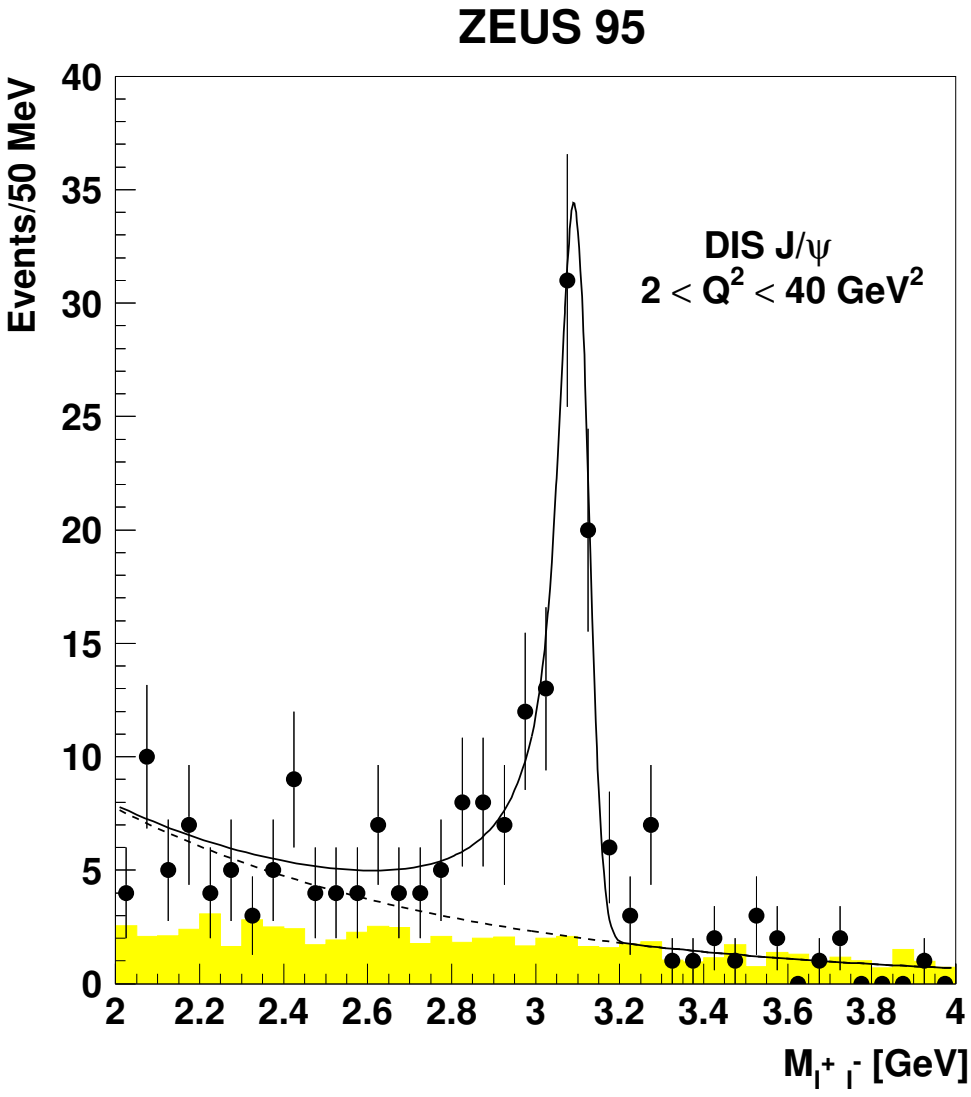

Figure 8: The differential mass distribution for the DIS J/ψ sample (not corrected for acceptance). The distribution includes contributions from both e^+e^- and $\mu^+\mu^-$ pairs. Solid line – signal function (see text), dashed line – background; shaded area – contribution from the Bethe-Heitler process.

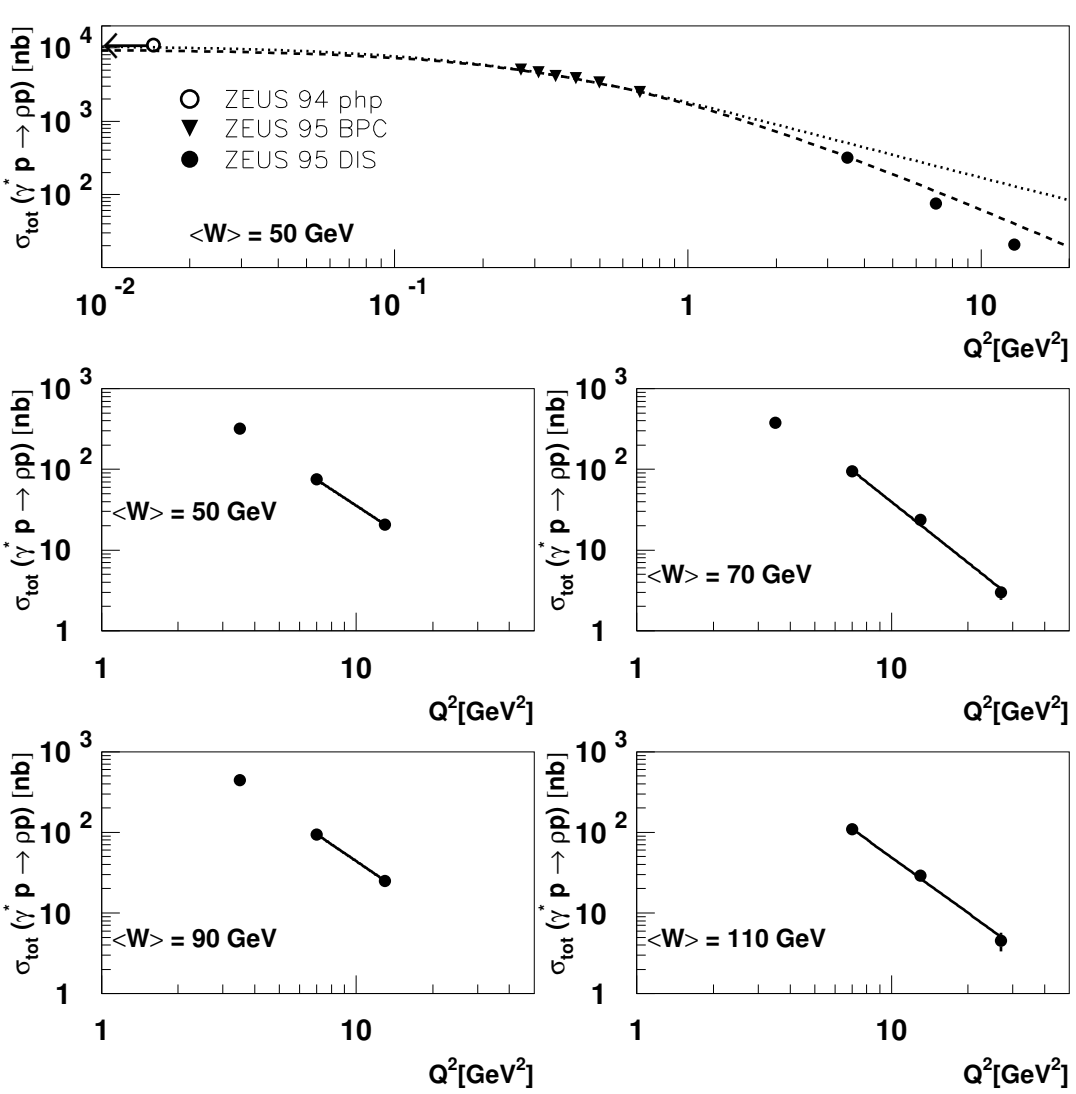

Figure 9: The cross sections, $\sigma_{\rm tot}^{\gamma^\star {\rm P}}$, for exclusive ρ^0 production as a function of Q^2 for various values of W. Top figure: the curves represent fits to the low-Q^2 (BPC) data using the functions $(1+R)/(1+Q^2/M_{\rm eff}^2)^2$ (dotted line) and $1/(1+Q^2/M_\rho^2)^n$ (dashed line). The open point with the horizontal arrow indicates the value measured in photoproduction [49]. Four bottom figures: the solid lines represent a fit of the form $\sigma_{\rm tot}^{\gamma^\star {\rm P}} \propto Q^{-2n}$ for $Q^2 > 5$ GeV^2. Only statistical uncertainties are shown.

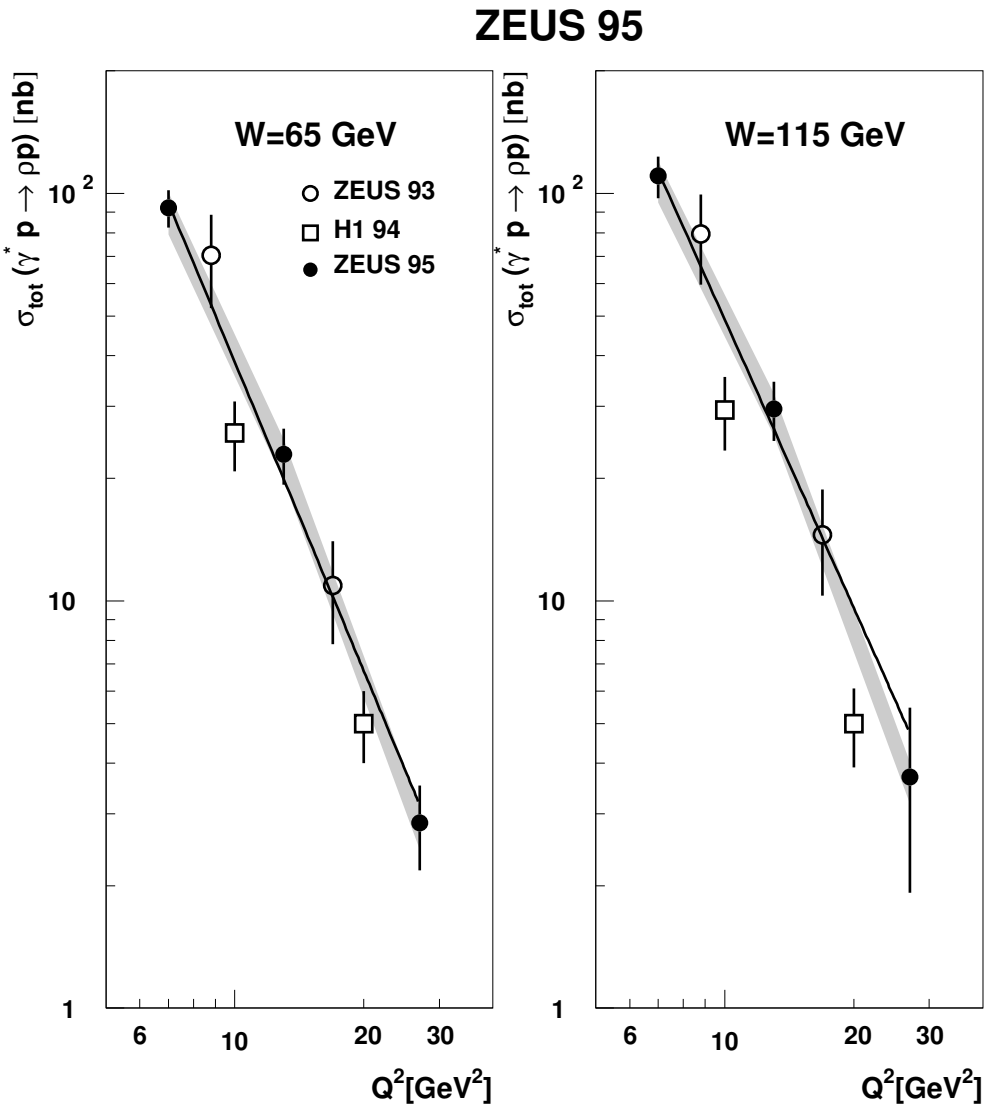

Figure 10: Comparison of the Q^2 dependence of $\sigma_{\rm tot}^{\gamma^\star {\rm p}}$ measured by ZEUS and H1. The ZEUS points were moved to the W values quoted for the H1 measurements. The lines represent the results of fits to ZEUS 95 data. The error bars on the ZEUS points represent the quadratic sum of statistical and systematic uncertainties. The normalisation uncertainties in the ZEUS measurements are indicated by the shaded areas.

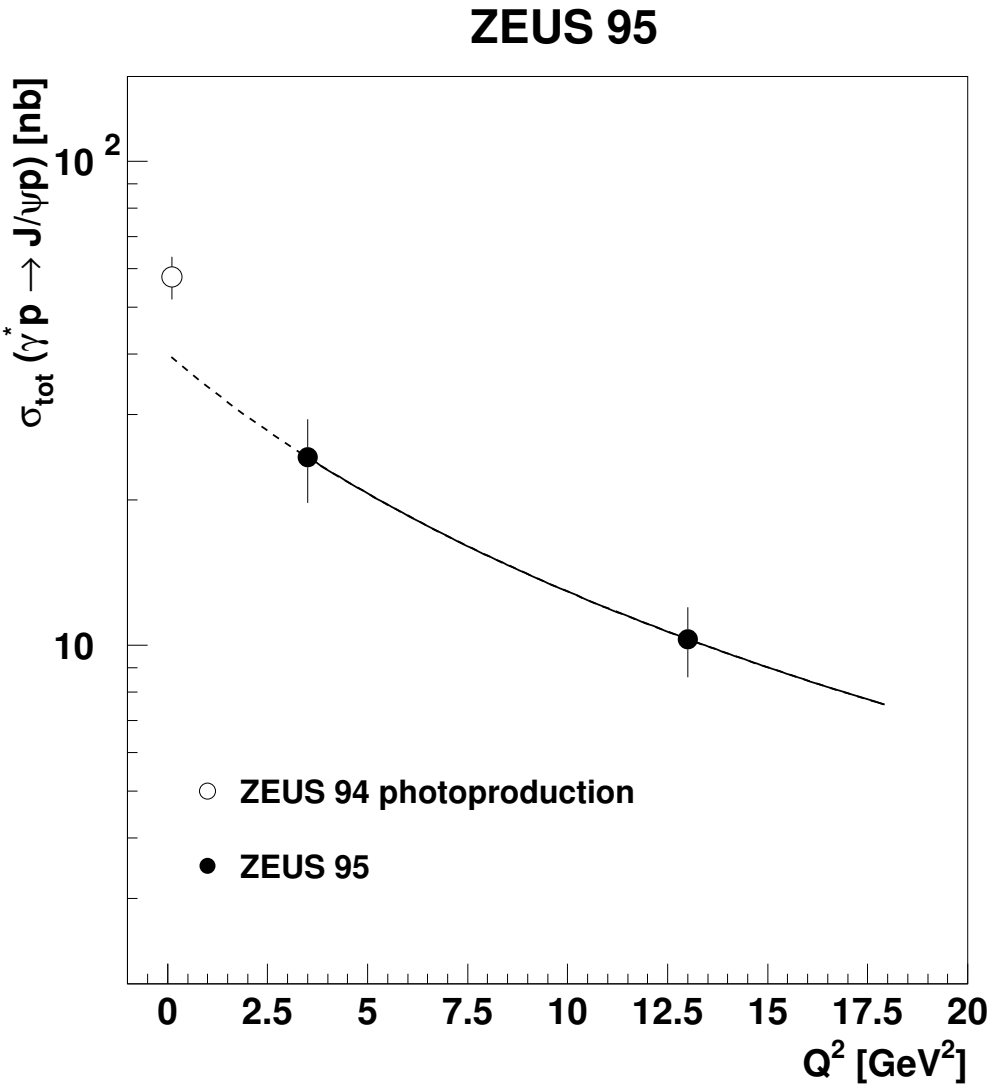

Figure 11: The cross section, $\sigma_{\rm tot}^{\gamma^\star {\rm p}}$, for exclusive J/ψ production as a function of Q^2. Line types: solid – function $\sigma_{\rm tot}^{\gamma^\star {\rm p}} \propto 1/(1+Q^2/M_{J/\psi}^2)^n$ fitted to the data points at Q^2=3 and 13 GeV^2; dashed – extrapolation of the fit result to Q^2=0. Only statistical errors are shown.

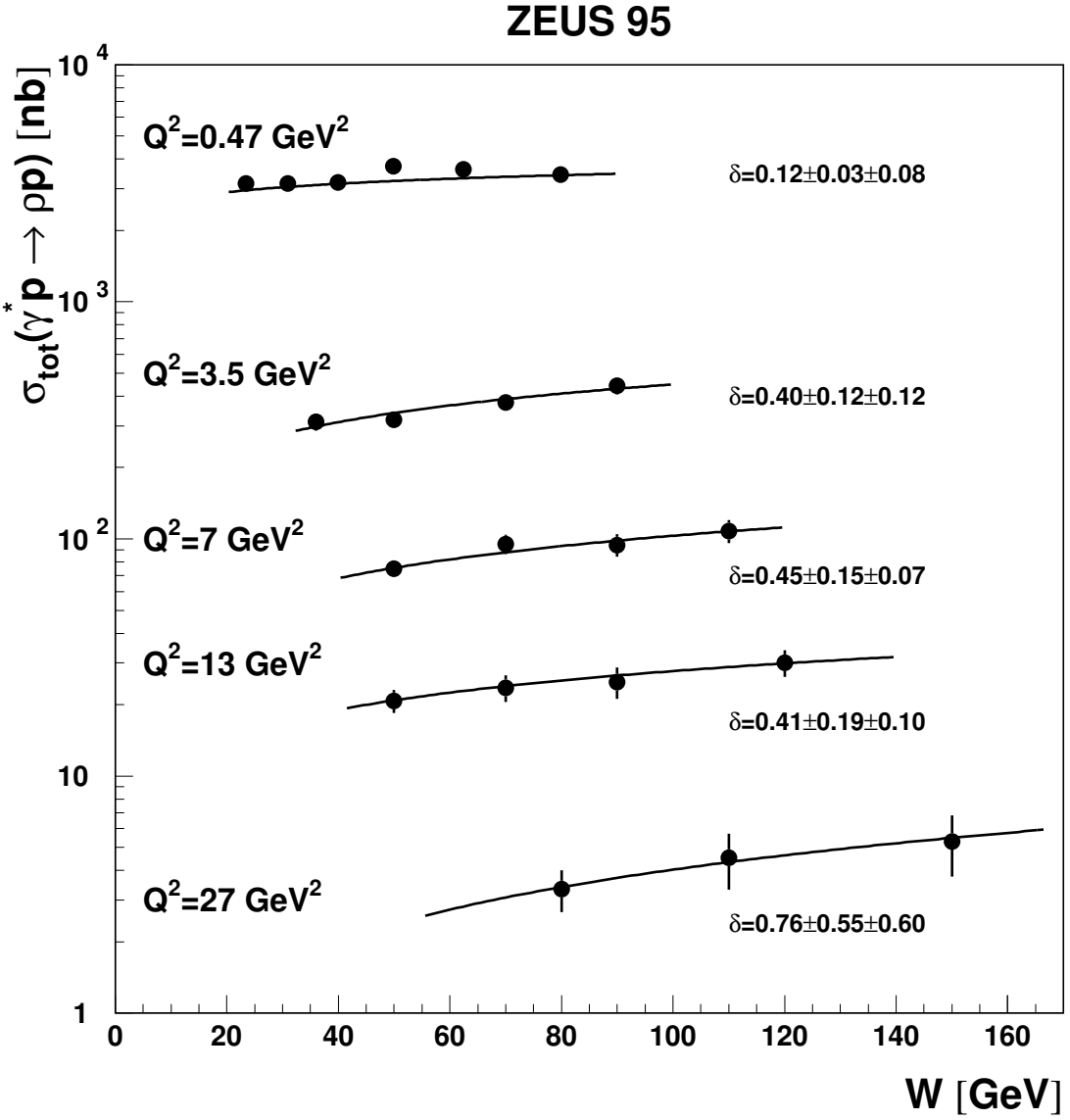

Figure 12: The cross section, $\sigma_{\rm tot}^{\gamma^* {\rm p}}$, for exclusive ρ^0 production as a function of W for various values of Q^2. Only statistical errors are shown. The lines represent the fitted parameterisation $\sigma_{\rm tot}^{\gamma^* {\rm p}} \propto W^{\delta}$.

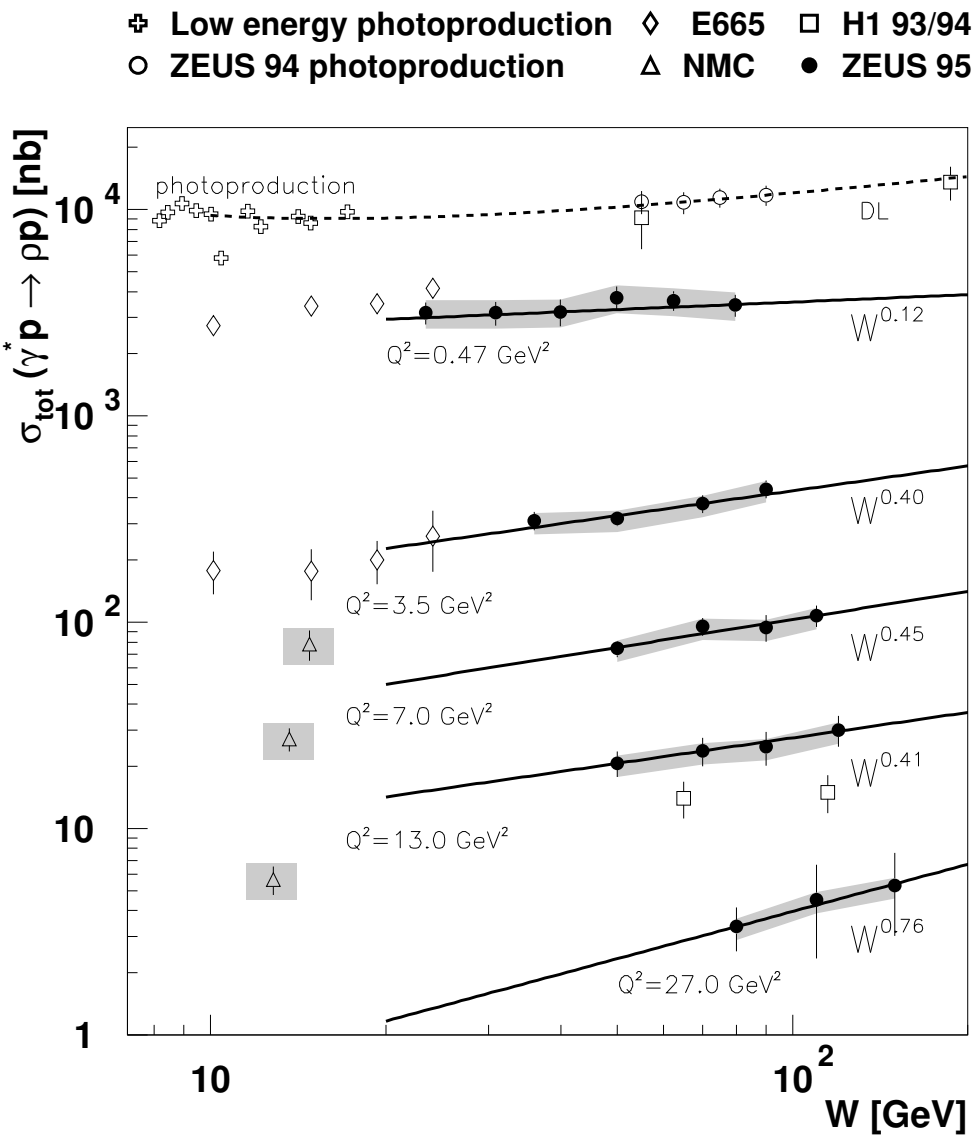

Figure 13: Comparison of cross sections, $\sigma_{\rm tot}^{\gamma^* {\rm p}}$, for exclusive ρ^0 production, as a function of W for various values of Q^2. The error bars represent statistical and systematic errors added in quadrature. The solid lines represent the fit results shown in Fig. 12. The dashed line is the prediction by Donnachie and Landshoff [8]. The overall normalisation uncertainties are shown as shaded bands for the NMC and ZEUS data points. The NMC [12], E665 [13] and H1 [15] data points were interpolated to the indicated Q^2 values (see text).

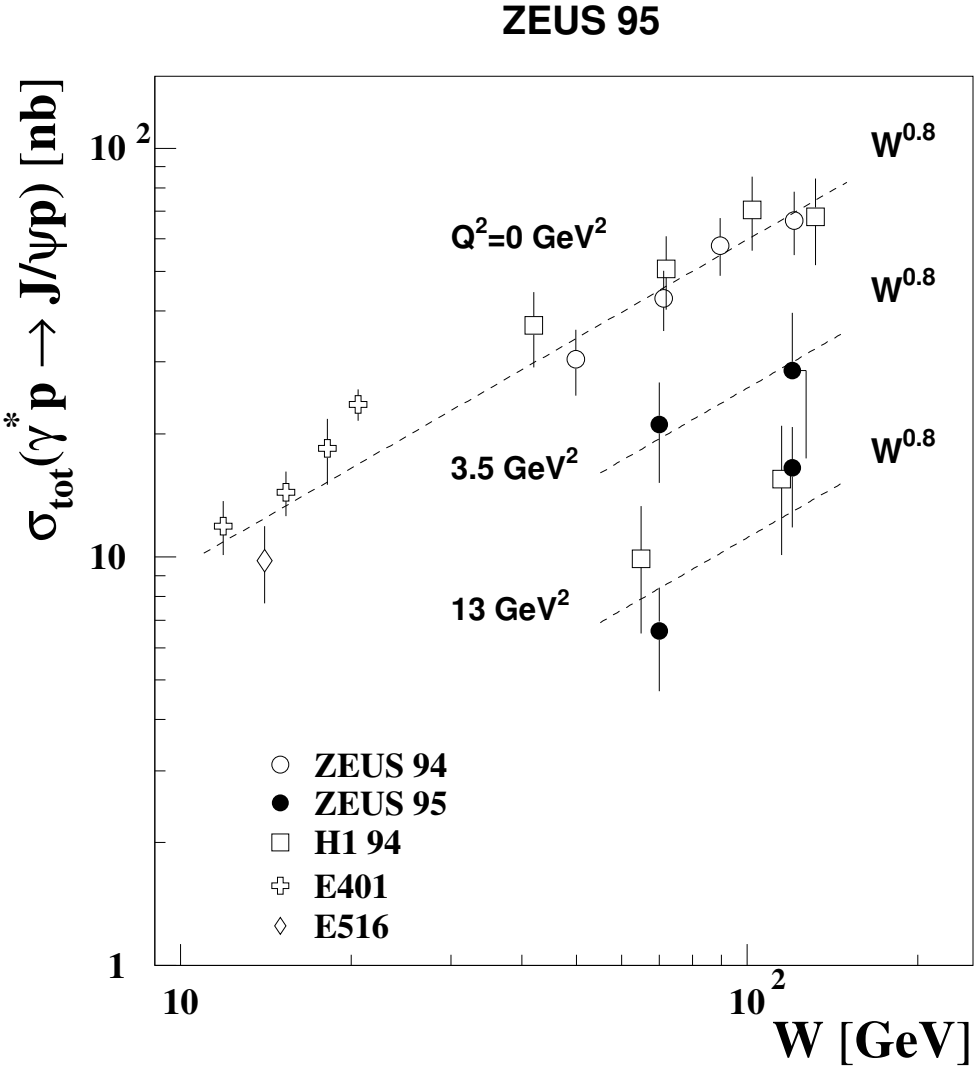

Figure 14: The cross section, $\sigma_{\rm tot}^{\gamma^* {\rm p}}$, for exclusive J/ψ production as a function of W for various values of Q^2. The error bars represent statistical and systematic uncertainties added in quadrature, including the normalisation uncertainty in the ZEUS measurements of $^{+13\%}_{-15\%}$. Measurements from the fixed target experiments, E401 [54] and E516 [55] are included for comparison. The lines, drawn to guide the eye, correspond to the cross section parameterisation $\sigma_{\rm tot}^{\gamma^* {\rm p}} \propto W^{0.8}$.

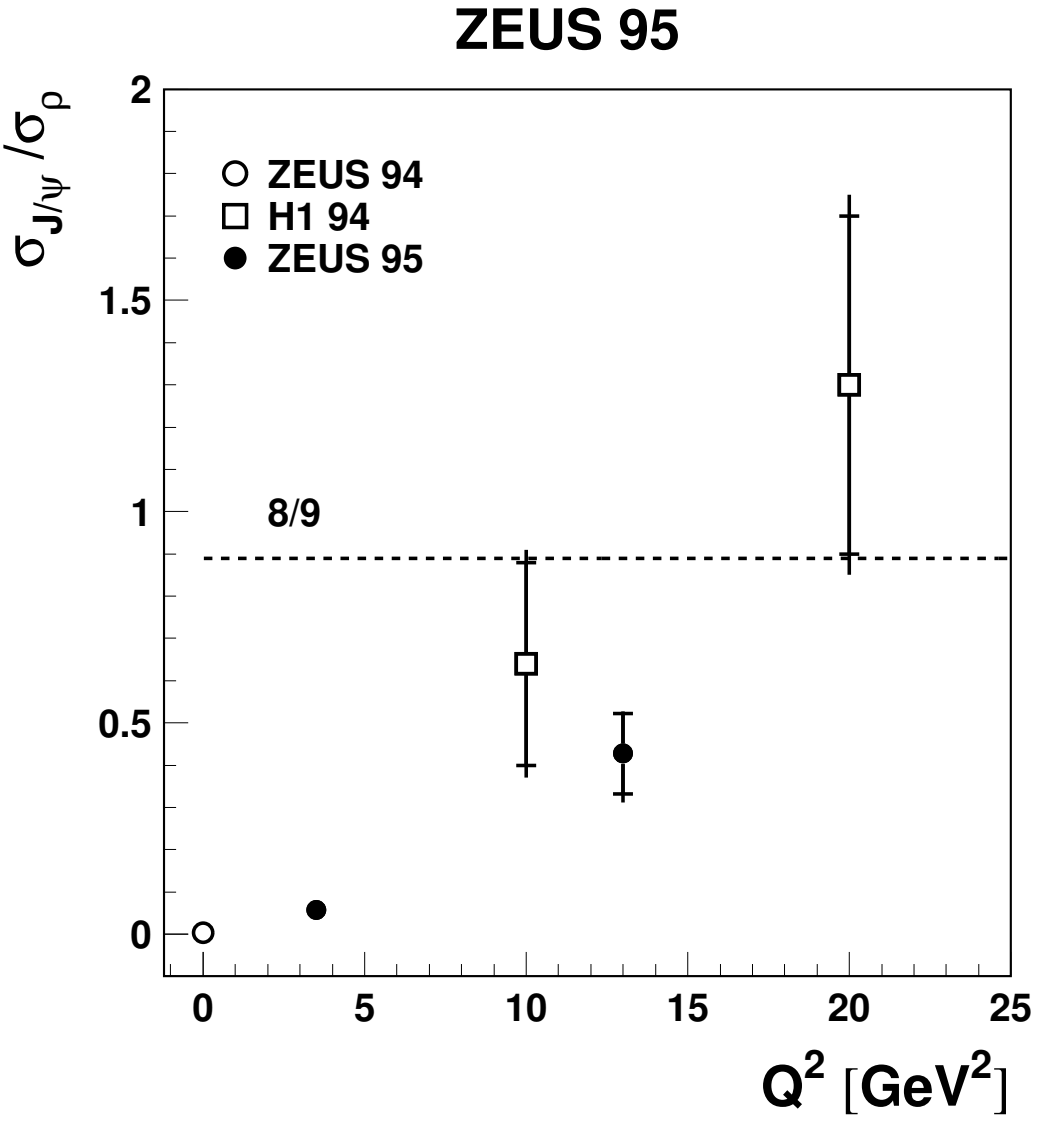

Figure 15: The ratio of the $\gamma^\star$p cross sections for exclusive J/ψ and ρ^0 production as a function of Q^2 [10, 15]. The dashed line indicates the flavour-symmetric expectation of 8/9. The inner error bars represent statistical uncertainties; the outer error bars indicate the quadratic sum of statistical and systematic uncertainties.

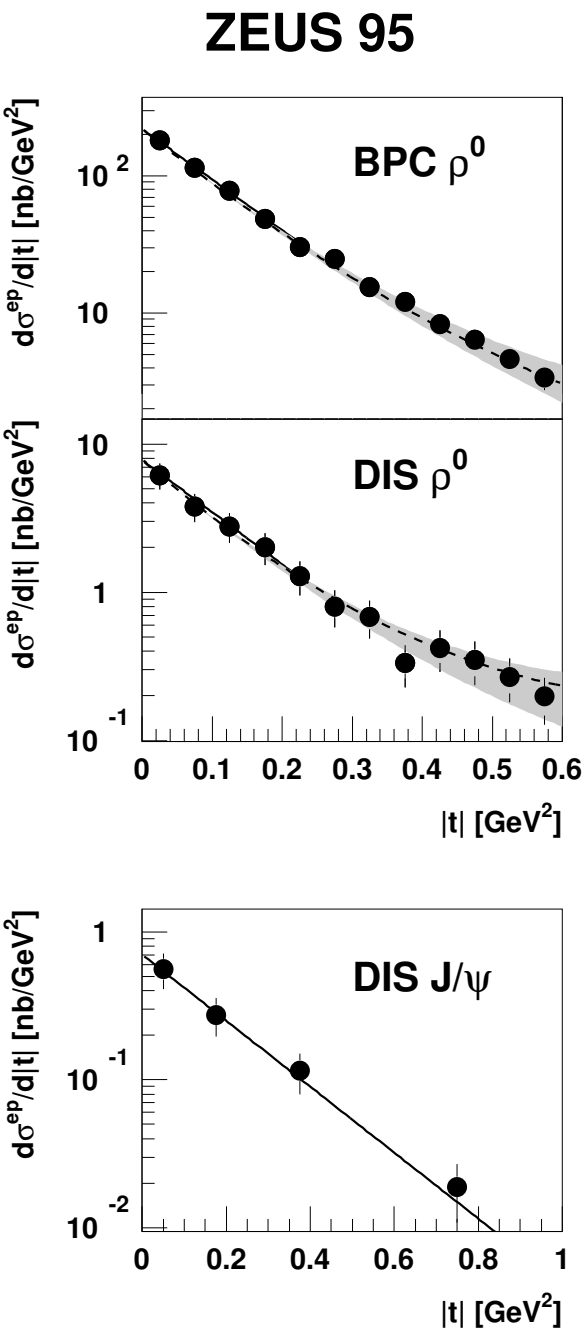

Figure 16: The differential cross section $\mathrm{d}\sigma^{\mathrm{ep}}/\mathrm{d}|t|$ for $\pi^+\pi^-$ ($0.6 < M_{\pi\pi} < 1.2$ GeV) and J/ψ production. Only statistical errors are shown. Line types: solid – fit of the function $\mathrm{d}\sigma^{\mathrm{ep}}/\mathrm{d}|t| \propto e^{-b|t|}$ for $|t| < 0.3$ GeV^2 ($|t| < 1$ GeV^2 for J/ψ); dashed – $\mathrm{d}\sigma^{\mathrm{ep}}/\mathrm{d}|t| \propto e^{-b|t|+ct^2}$ for $|t| < 0.6$ GeV^2; the shaded band indicates the systematic error resulting from the uncertainty in the parameter c.

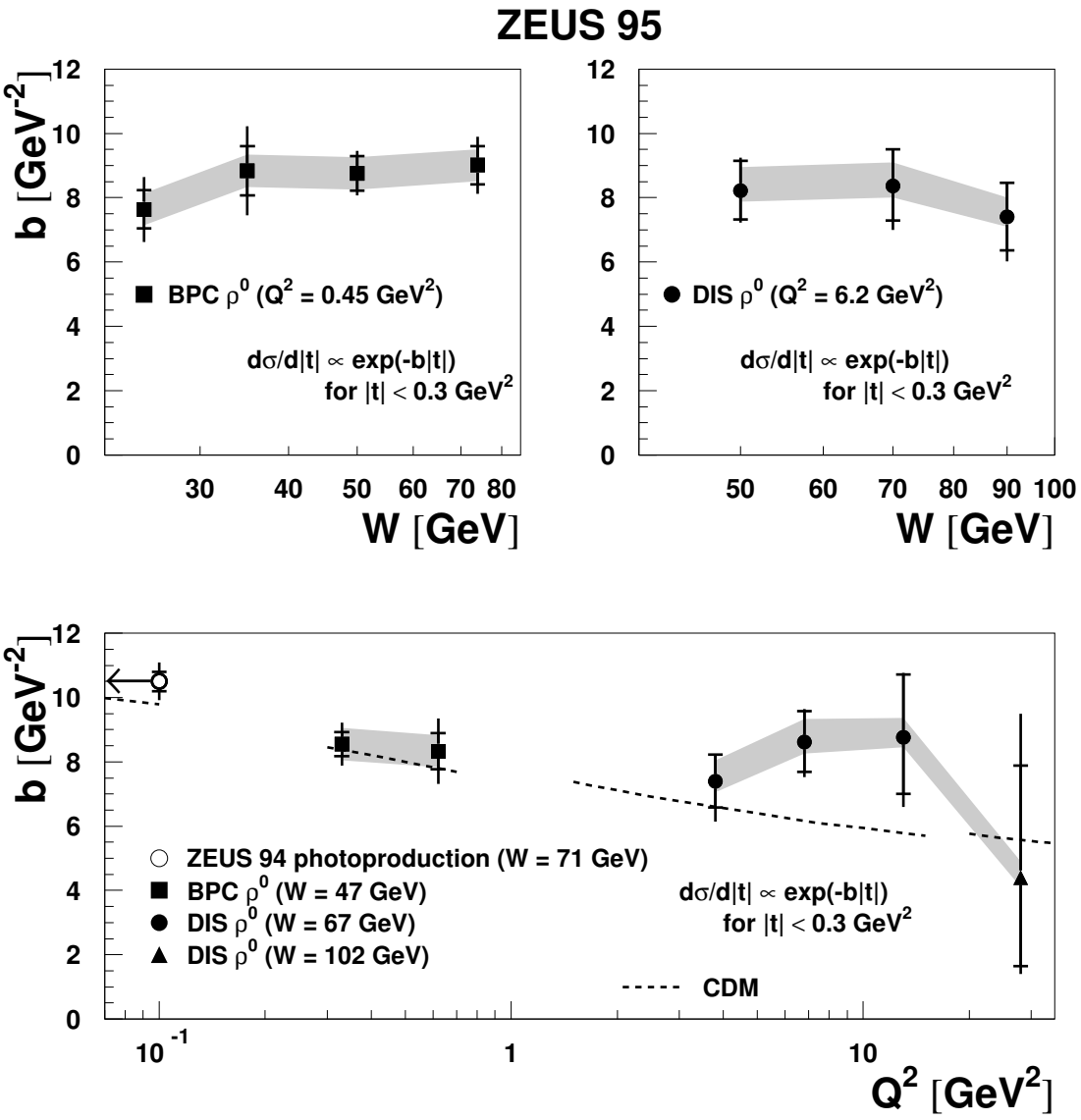

Figure 17: The slope parameter b as a function of W and Q^2 for exclusive $\pi^+\pi^-$ production (BPC and DIS samples) in the range $0.6 < M_{\pi\pi} < 1.2$ GeV. The open point with the horizontal arrow indicates the value measured in photoproduction [49]. The inner error bars represent statistical uncertainties; the outer error bars indicate the quadratic sum of statistical and systematic uncertainties. The shaded areas indicate additional normalisation uncertainties due to the proton dissociation background subtraction. The dashed lines represent predictions of the Colour Dipole Model (CDM) of Nemchik et al. [20] at the corresponding Q^2 and W values.

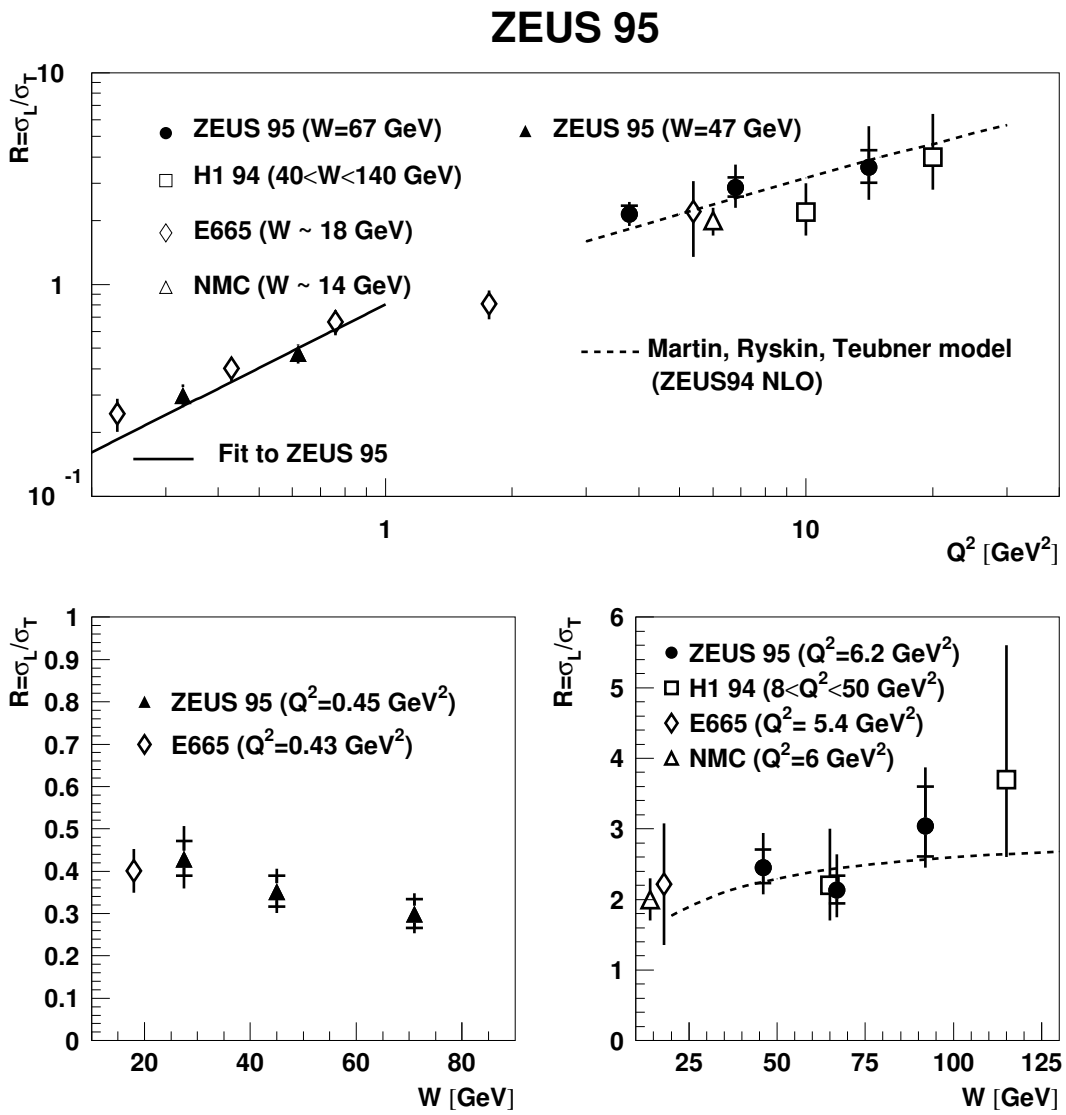

Figure 18: The ratio of the cross sections for longitudinal and transverse photons, $R = \sigma_{\rm L}^{\gamma^* {\rm p}}/\sigma_{\rm T}^{\gamma^* {\rm p}}$, for exclusive $\pi^+\pi^-$ production in the range $0.6 < M_{\pi\pi} < 1.2$ GeV as a function of Q^2 and W, evaluated assuming SCHC. The inner error bars represent statistical uncertainties; the outer error bars indicate the quadratic sum of statistical and systematic uncertainties. The solid line represents the result of a fit to the BPC data of the form $R = \kappa Q^2$, which yielded $\kappa = 0.81 \pm 0.05({\rm stat.}) \pm 0.06({\rm syst.})$. The dashed line is a prediction of the model by Martin, Ryskin and Teubner [27] using the ZEUS 94 NLO parameterisation of the gluon density [56].

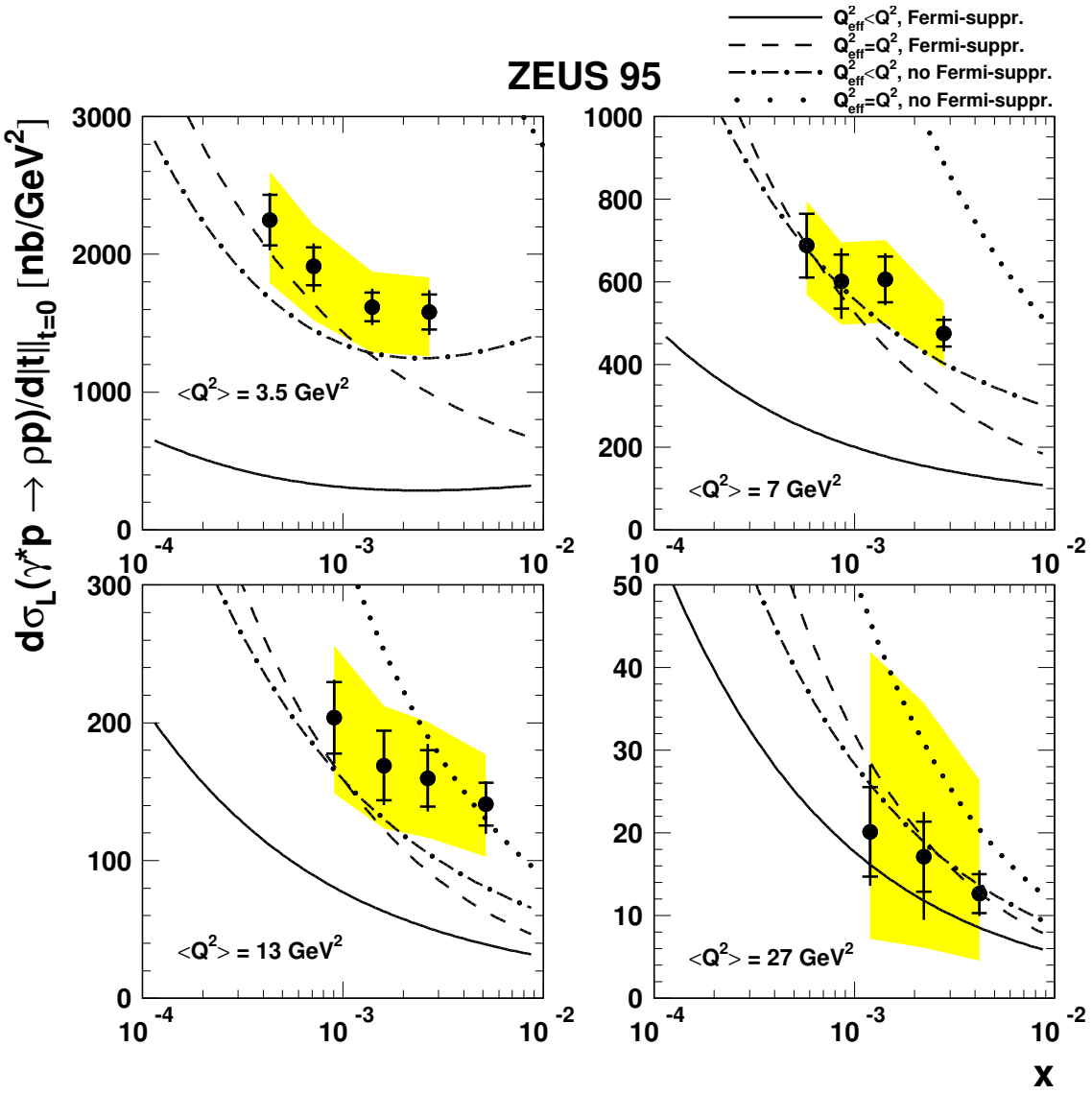

Figure 19: The measured forward longitudinal cross section, $\mathrm{d}\sigma_{\mathrm{L}}^{\gamma^* \mathrm{p}}/\mathrm{d}|t|\Big|_{t=0}$, as a function of x for the DIS ρ^0 sample. The inner error bars represent statistical uncertainties; the outer error bars indicate the quadratic sum of statistical and systematic uncertainties. The shaded areas indicate additional normalisation uncertainties due to the proton dissociation background subtraction as well as the measured values of the $R = \sigma_{\mathrm{L}}^{\gamma^* \mathrm{p}}/\sigma_{\mathrm{T}}^{\gamma^* \mathrm{p}}$ ratio and the slope parameter b. The curves show the predictions by Frankfurt, Koepf and Strikman [25] using the ZEUS 94 NLO gluon parameterisation [56]. The full and dashed lines show the result of the calculation assuming hard Fermi suppression with rescaling ($Q^2_{\mathrm{eff}} < Q^2$) and without rescaling ($Q^2_{\mathrm{eff}} = Q^2$). The dashed-dotted and dotted lines show the result assuming no hard Fermi suppression with and without rescaling.

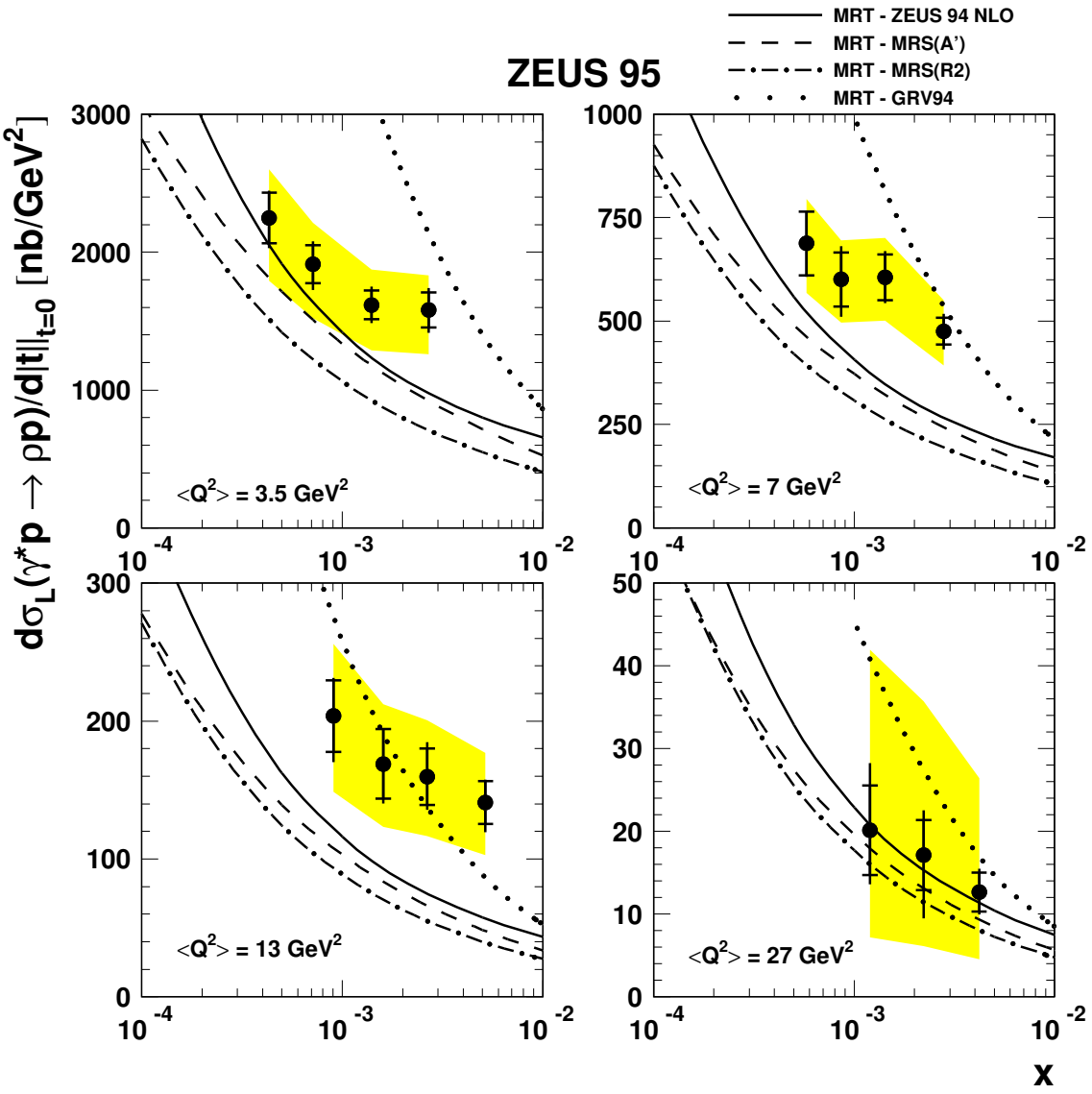

Figure 20: The measured forward longitudinal cross section, $\mathrm{d}\sigma_{\mathrm{L}}^{\gamma^* \mathrm{p}}/\mathrm{d}|t|\Big|_{t=0}$, as a function of x for the DIS ρ^0 sample. The inner error bars represent statistical uncertainties; the outer error bars indicate the quadratic sum of statistical and systematic uncertainties. The shaded areas indicate additional normalisation uncertainties due to the proton dissociation background subtraction as well as the measured values of the $R = \sigma_{\mathrm{L}}^{\gamma^* \mathrm{p}}/\sigma_{\mathrm{T}}^{\gamma^* \mathrm{p}}$ ratio and the t-slope parameter b. The curves show the predictions by Martin, Ryskin and Teubner [27] and correspond to various gluon parameterisations, indicated as follows: full lines – ZEUS 94 NLO [56], dashed lines – MRSA′ [43], dashed-dotted lines – MRSR2 [57], and dotted lines – GRV94 [58].

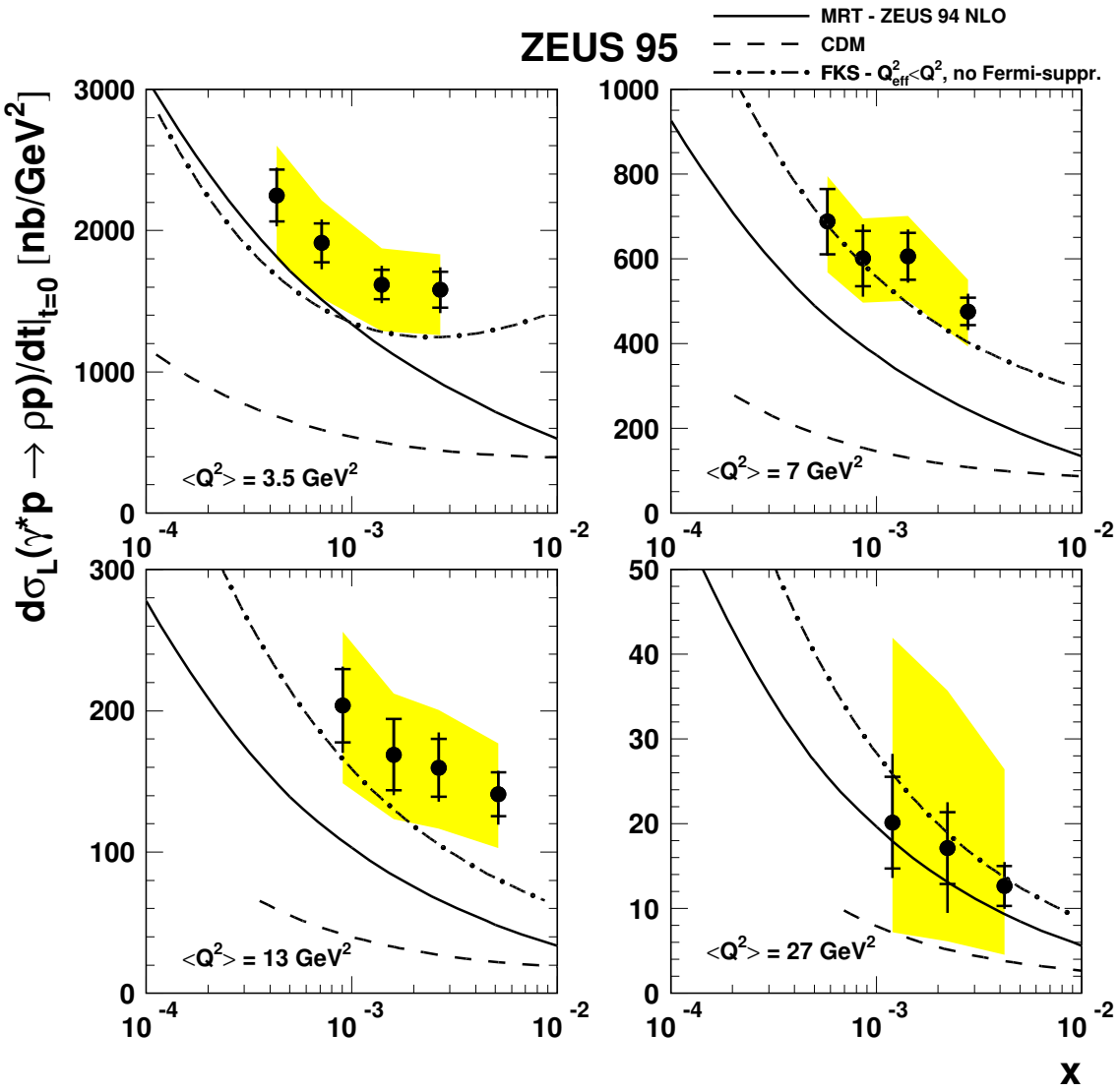

Figure 21: The measured forward longitudinal cross section, $\mathrm{d}\sigma_{\mathrm{L}}^{\gamma^*\mathrm{p}}/\mathrm{d}|t|\Big|_{t=0}$, as a function of x for the DIS ρ^0 sample. The inner error bars represent statistical uncertainties; the outer error bars indicate the quadratic sum of statistical and systematic uncertainties. The shaded areas indicate additional normalisation uncertainties due to the proton dissociation background subtraction as well as the measured values of the $R = \sigma_{\mathrm{L}}^{\gamma^*\mathrm{p}}/\sigma_{\mathrm{T}}^{\gamma^*\mathrm{p}}$ ratio and the slope parameter b. The solid line shows the calculation by Martin, Ryskin and Teubner [27] using the ZEUS 94 NLO gluon density parameterisation. The dashed line shows the result of a calculation using CDM [20]. The dashed-dotted line shows the prediction of Frankfurt, Koepf and Strikman [25] using the ZEUS 94 NLO gluon parameterisation with rescaling ($Q^2_{\mathrm{eff}} < Q^2$) and no hard Fermi suppression.